




# High-fidelity simulation of a hydraulic jump around a surface-piercing hydrofoil

Cite as: Phys. Fluids **33**, 123304 (2021); <https://doi.org/10.1063/5.0074943>

Submitted: 12 October 2021 • Accepted: 07 November 2021 • Published Online: 02 December 2021

 Zheng Li (李政),  Cheng Liu (刘成),  Decheng Wan (万德成), et al.

## COLLECTIONS

 This paper was selected as an Editor's Pick



View Online



Export Citation



CrossMark

Physics of Fluids

SPECIAL TOPIC: Flow and Acoustics of Unmanned Vehicles

Submit Today!



# High-fidelity simulation of a hydraulic jump around a surface-piercing hydrofoil

Cite as: Phys. Fluids **33**, 123304 (2021); doi: [10.1063/5.0074943](https://doi.org/10.1063/5.0074943)

Submitted: 12 October 2021 · Accepted: 7 November 2021 ·

Published Online: 2 December 2021




View Online



Export Citation



CrossMark

Zheng Li (李政),<sup>1</sup>  Cheng Liu (刘成),<sup>1,a)</sup>  Decheng Wan (万德成),<sup>1</sup>  and Changhong Hu (胡长洪)<sup>2</sup> 

## AFFILIATIONS

<sup>1</sup>Computational Marine Hydrodynamics Lab (CMHL), School of Naval Architecture, Ocean and Civil Engineering, Shanghai Jiao Tong University, Shanghai 200240, China

<sup>2</sup>Research Institute for Applied Mechanics, Kyushu University, Fukuoka 816-0811, Japan

<sup>a)</sup> Author to whom correspondence should be addressed: [chengliu@sjtu.edu.cn](mailto:chengliu@sjtu.edu.cn)

## ABSTRACT

For a surface-piercing hydrofoil traveling at high speed, a turbulent hydraulic jump may arise at the intersection of the body with the free surface. This hydrodynamic phenomenon involves violent wave breaking, bringing great challenges for experimental analysis. In this work, a high-fidelity large eddy simulation is performed to study the turbulent air-entraining flow near foil. One advantage of the present simulation is that a quantitative analysis can be implemented even in the turbulent two-phase mixing region containing a large amount of entrained air, which is difficult for traditional experimental and theoretical approaches. We employ a conservative coupled level set/volume-of-fluid scheme to capture the free surface. A highly robust scheme is introduced to guarantee stability in simulating large density ratio two-phase flows. The present method is implemented based on a block-structured adaptive mesh, by which the efficiency of the high-fidelity simulation can be improved. The main flow features of the wedge-shaped hydraulic jump, including the wave patterns, free surface elevation, and frequency spectra, are compared with experimental data. We find that the flow structures show clear differences from those found in the canonical hydraulic jump, owing to the presence of the foil surface. Shoulder wave breaking starts at the trough of the mid-body, develops in a wedge shape, depends strongly on Froude number, and is responsible for most of the large-scale air entrainment. The properties of the turbulent hydraulic jump and some of the key quantities characterizing the air-entraining flow, including the spatial distribution of the bubble cloud, the void fraction, and the bubble/droplet size spectrum, are fully investigated for typical Froude numbers.

Published under an exclusive license by AIP Publishing. <https://doi.org/10.1063/5.0074943>

## I. INTRODUCTION

Hydraulic jumps are commonly observed in natural streams, open channels, and man-made water conveyance systems, and often occur when bulk volumes of high-velocity water discharge into lower-velocity regions. The abruptly slowed volume of water causes a significant increase in wave height. Turbulent hydraulic jumps, characterized by wave breaking and strong air–water mixing, are usually encountered at high inflow velocities (Froude number  $Fr > 2.5$ ).<sup>1</sup>

However, for flow past a semi-submerged structure with long draft and blunt bow (e.g., a NACA 0024 foil), the presence of the blunt bow changes the velocity distribution around the body, stimulating a special wedge-shaped hydraulic jump adjacent to the body, with no obvious characteristic length scale.<sup>2</sup> The wedge-shaped region forming behind the bow wave trough contains more complicated hydrodynamic phenomena, including three-dimensional wave breaking with intense free-surface fluctuations, droplet splashing, and air entrainment.<sup>2,3</sup> The aim of the present study is to clarify the mechanisms involved in the formation of hydraulic jumps and the associated two-

phase flow characteristics by means of high-fidelity numerical simulations.

There have been extensive studies of canonical air–water hydraulic jumps [Fig. 1(b)].<sup>4–8</sup> For the turbulent hydraulic jump regions generated by breaking waves, four types of subregions can be identified:<sup>4</sup> the boundary layer region, the potential core region, the mixing layer region, and the recirculation region [Fig. 1(b)]. Similar flow patterns can also be recognized in the wedge-shaped hydraulic jumps arising from free-surface flow past a NACA foil [Fig. 1(a)]. In the recirculation region (also referred to as the roller region<sup>5</sup>), overturning of the wave-front and subsequent splashing in the reverse direction produce large swirling vortices, intense spray, and significant air entrainment. Air bubbles and pockets, which are entrapped into the turbulent roller owing to the impingement of high-velocity inflow, will be advected in the developing mixing layer.<sup>6</sup> Using conductivity measurements, Chachereau and Chanson<sup>5</sup> found that both the void fraction and the bubble count rate reach maxima in the mixing layer region. The highly aerated flow brings difficulties for any detailed analysis of instantaneous

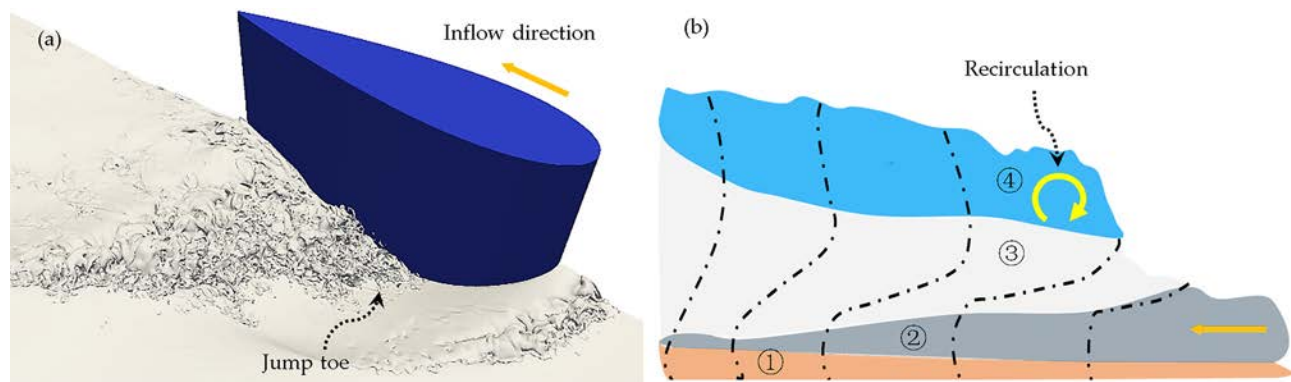


**FIG. 1.** Sketches of hydraulic jumps. (a) Wedge-shaped hydraulic jump adjacent to a NACA foil, where the instantaneous free surface is extracted with volume fraction  $C = 0.5$ . (b) Canonical hydraulic jump with four characteristic regions: ① boundary layer; ② potential core; ③ mixing layer; ④ recirculation region. The dotted–dashed lines are horizontal velocity profiles at different downstream positions.

flow features. Bubble image velocimetry (BIV)<sup>4,7</sup> is often employed for analysis of turbulence statistics and for tracking large-scale bubbles (i.e., trajectory, velocity, velocity fluctuations, etc.). Rodríguez-Rodríguez *et al.*<sup>7</sup> studied the evolution of coherent vortices in the aerated region. They found that the large eddy generated near the jump toe will move downstream with nearly constant velocity. Vortex size grows linearly, and the growth rate is limited due to the presence of a free surface. Lin *et al.*<sup>4</sup> summarized the characteristics of bubble dynamics and found the time-averaged horizontal bubble velocities to be lower than the water velocity owing to drag caused by shear forces.

Experimental techniques provide efficient means for understanding the general flow characteristics of turbulent hydraulic jumps. However, owing to the difficulty in capturing and tracking moving bubbles (with deformation), accurate and credible experimental analysis of instantaneous bubble–water interactions remains a great challenge. Besides, the instantaneous air entrainment and related small-scale three-dimensional (3D) flow structures are also extremely hard to visualize and analyze systematically. These difficulties have led to an insufficient understanding of the fundamental mechanisms of bubble–water interactions in the highly aerated region.

In the wedge-shaped hydraulic jump region around a surface-piercing foil, flow structures are fairly abundant [Fig. 1(a)], but corresponding studies on the inner relationship between instantaneous flow features and air entrainment are rare in the literature. Most of the relevant works have focused on the flow separation induced by free-surface waves. Chow<sup>9</sup> studied this phenomenon experimentally and found that the separation is initiated beyond the bow wave trough and extended to the trailing edge. A subsequent experimental fluid dynamics (EFD) study of a surface-piercing flat plate<sup>10</sup> also proved the existence of flow separation, indicated by a wedge-shaped after-body region near the free surface. An experiment by Metcalf *et al.*<sup>3</sup> revealed the frequency spectra of the unsteady near-field free-surface elevation and the foil-surface pressure, with three dominant periodic modes being quantitatively identified, corresponding to the shear layer, Kármán vortex shedding, and flapping instabilities, respectively. EFD study based on particle image velocimetry techniques (PIV) study providing insight into the flow field was carried out by Pogozelski *et al.*,<sup>2</sup> who concluded that the separation process originates from secondary flows associated with impingement and breaking at the root of

the shoulder wave. The separated region consists of streamwise counter-rotating vortex pairs detached from the boundary layer on the body, which strongly affects the distribution of large-scale bubble clouds below the free surface. The present study shows that the distribution of internal two-phase flow characteristics and the air entrainment behavior both depend heavily on the occurrence of flow separation near the foil, which is different from the canonical hydraulic jump in a water channel.

Although there have been some numerical simulations of the free-surface flow around a surface-piercing structure,<sup>11–13</sup> they have focused on the hydrodynamic force rather than the development of the bubbly wake, in which case the use of turbulent model based on the unsteady, single-phase Reynolds-averaged Navier–Stokes (URANS) equations<sup>11</sup> is adequate. To elucidate the hydrodynamic process of large-scale air entrainment and reveal the evolution of the dominant flow structures in the hydraulic jump region, numerical analysis with high spatial and temporal resolutions is necessary. Mortazavi *et al.*<sup>14</sup> conducted direct numerical simulation (DNS) of a canonical hydraulic jump and quantified the correlation between bubble formation and coherent vortex structures generated by semi-periodic wave breaking. Autocorrelation of submerged air volume downstream of the jump reveals a frequency consistent with the dominant frequency of the velocity energy spectrum. Since the turbulent hydraulic jump phenomenon may be partially interpreted in terms of a wave breaking process,<sup>14</sup> numerical work related to plunging wave breaking<sup>15–20</sup> and free-surface flow around submerged structures<sup>21–23</sup> can be used as reference. Liu *et al.*<sup>24</sup> summarized recent advances in the simulation of breaking waves and found that most of investigations have focused on DNS of centimeter-scale wave breaking problems, with quantitative analyses of vortex structures,<sup>17</sup> air entrainment,<sup>15,16</sup> and surface tension effects.<sup>25</sup> For the case of a surface-piercing foil interacting with a free surface, turbulence anisotropy due to boundary layer or flow separation induces more coherent structures, which have important effects on the entrainment mechanism.<sup>26,27</sup> However, the air entrainment characteristics and the relationship between the nonuniform turbulent dissipation field and the bubble size distribution are still unclear. Besides, from the perspective of numerical methods, whereas high-fidelity simulations show potential for revealing the fundamental physics of hydraulic jumps,<sup>14</sup>

traditional fixed mesh refinement strategies with nonconservative or low-order schemes introduce redundant dissipation and are inadequate to simulate bubble-laden turbulent flow.

In this work, a block-structured adaptive mesh refinement (BAMR) strategy<sup>28–30</sup> is applied to improve the efficiency of large-scale parallel computations, with grids being dynamically refined around the interface and body surface region. To reproduce the main flow structures accurately with less numerical dissipation, a fifth-order weighted essentially non-oscillatory (WENO) method is adopted. A coupled level set/volume-of-fluid (CLSVOF) scheme<sup>31</sup> together with a high-robustness mass–momentum consistent advection algorithm<sup>32</sup> is implemented to ensure stability in the simulation of two-phase flows with a large density ratio. By using these approaches, the formation of a turbulent hydraulic jump and the general flow features can be simulated accurately.

Our simulation reproduces crucial characteristics involved in turbulent hydraulic jumps, including the shoulder wave breaking initiated at the bow wave trough, the overturning jet and subsequent splashing (major sources for air entrainment), and wave-induced flow separation near the after-body of the hydrofoil. We investigate the characteristics of wedge-shaped hydraulic jumps at different Froude numbers, including the instantaneous and time-averaged wave patterns, the mean flow field in complex air–water mixed regions. Although the shear layer is similar to that of a canonical hydraulic jump [Fig. 1(b)], as can be identified in the mixed regions, the presence of three-dimensional shoulder wave breaking and the associated flow separation leads to unique flow patterns. A bubble/droplet detection program is developed to quantify the features of air entrainment. The spatial distribution of bubble clouds, the time-averaged volume fraction, and the surface entrainment rate are obtained and analyzed in detail.

The highlights of the present study are as follows:

1. A high-fidelity numerical simulation based on an efficient adaptive mesh strategy is performed to simulate the turbulent hydraulic jump around a NACA foil.
2. We explore the intrinsic factors that may affect the formation and evolution of a wedge-shaped hydraulic jump, and we find that the flow structures are significantly different from those associated with canonical hydraulic jumps, owing to the presence of the foil.
3. This is the first attempt to quantitatively analyze air entrainment by a surface-piercing NACA foil using simulations. Some of the important characteristics of the bubble clouds, including the spatial and temporal distribution, total volume, and size spectrum, are investigated numerically.

The remainder of the paper is organized as follows. Section II details the computational method, including the governing equations and numerical strategies. Section III presents the computational configurations and comparisons with EFD measurements. Section IV analyzes the formation and evolution of hydraulic jumps and the time-averaged flow features. Large-scale air entrainment behavior is discussed in detail in Sec. V. Finally, the main conclusions of this work are summarized in Sec. VI.

## II. COMPUTATIONAL METHOD

### A. Governing equations

The governing equations describing unsteady incompressible two-phase flows can be written in a conservative form as follows:

$$\frac{\partial \rho}{\partial t} + \nabla \cdot (\rho \mathbf{u}) = 0, \tag{1a}$$

$$\frac{\partial (\rho \mathbf{u})}{\partial t} + \nabla \cdot (\rho \mathbf{u} \mathbf{u}) = -\nabla p + \nabla \cdot \boldsymbol{\tau} + \rho \mathbf{g} + \mathbf{F}_S. \tag{1b}$$

Here,  $\mathbf{u}$  is the velocity vector,  $p$  is the pressure,  $\boldsymbol{\tau} = \mu[\nabla \mathbf{u} + (\nabla \mathbf{u})^T]$  is the shear stress tensor, and  $\mathbf{g}$  is the gravitational acceleration.  $\mu$  and  $\rho$  are the dynamic viscosity and the density of the fluid, which can be determined using the volume fraction  $C$  as

$$\rho = \rho_l C + \rho_g (1 - C), \quad \mu = \mu_l C + \mu_g (1 - C), \tag{2}$$

where the subscripts  $l$  and  $g$  indicate the liquid and gas phases, respectively. The surface tension  $\mathbf{F}_S$  is expressed as

$$\mathbf{F}_S = \sigma \kappa \delta_s \mathbf{n}, \tag{3}$$

where  $\sigma$  is the surface tension coefficient (assumed to be constant),  $\kappa$  is the local curvature of the interface, which is estimated by the height-function (HF)<sup>33</sup> method,  $\delta$  is the Dirac distribution function, and  $\mathbf{n}$  is the unit normal of the interface.

The motion and deformation of the interface are obtained by solving the passive-scalar transport equation,

$$\frac{\partial C}{\partial t} + \mathbf{u} \cdot \nabla C = 0, \tag{4}$$

where  $\mathbf{u}$  is the ambient velocity field,  $C$  is the volume fraction defined by

$$C = \frac{1}{V} \int_{\Omega} f(\mathbf{x}) d\mathbf{x}, \tag{5}$$

$f(\mathbf{x})$  is the Heaviside function, representing the interface profile. In this study, a geometrical VOF method based on the piecewise-linear interface calculation (PLIC) is implemented.

The present PLIC-VOF method is coupled with the level-set method to improve the shape-preserving property in capturing the interface. A transport equation [Eq. (6)] and a re-initialization equation [Eq. (7)] are solved alternatively for the signed distance function  $\phi$ . Therefore, the signed distance field ( $\phi$ ) rather than the volume fraction ( $C$ ) is utilized for linear reconstruction of the interface,<sup>31</sup>

$$\frac{\partial \phi}{\partial t} + \mathbf{u} \cdot \nabla \phi = 0, \tag{6}$$

$$\frac{\partial \phi}{\partial t} + \text{sgn}(\phi^0)(|\nabla \phi| - 1) = 0, \tag{7}$$

where  $\text{sgn}$  is the smoothed signed distance function.

For large eddy simulation (LES), vortices larger than the filter width are fully resolved, while small-scale eddies are modeled with a subgrid model. The subgrid-scale (SGS) stress tensor in LES is calculated by the Smagorinsky eddy viscosity model.<sup>34</sup>

### B. Numerical methods

The high-fidelity simulations are performed with the in-house code BAMR-SJTU, which is designed for the large-scale parallel computation of violent two-phase flow problems. Crucial numerical methodologies in the implementation of BAMR-SJTU are summarized here.

**TABLE I.** Parameters for three typical cases (A1, A2, and A3) originating from the experimental setups.<sup>3</sup>

Case	Fr	Re	Inflow velocity $U$ (m/s)	Draft $d$ (m)
A1	0.19	$8.04 \times 10^5$	0.67	1.5
A2	0.37	$1.52 \times 10^6$	1.27	1.5
A3	0.55	$2.26 \times 10^6$	1.89	1.5

The governing equations are discretized based on a staggered mesh configuration. A classical projection method<sup>35</sup> is applied to decouple the velocity and pressure.

To improve robustness in the simulation of high-density-ratio two-phase flow problems, a mass and momentum consistent advection method based on the early formulation proposed by Rudman<sup>36</sup> is developed for the staggered mesh. Instead of employing sub-grids computations of the volume fraction to construct the mass flux, in the present implementation the mass transport equation (1a) is solved with an upwind scheme to update the density field, and then the mass fluxes  $\rho \mathbf{u}$  that is required in solving the transport of momentum are derived accordingly. With this treatment, the mass and momentum equations are solved in a consistent manner, and incorrect transport of momentum adjacent to the interface can be avoided. Therefore, the spurious velocities and unphysical deformations of the interface often encountered in the simulation of violent two-phase flows are eliminated, and numerical stability is preserved.

We apply an efficient immersed boundary (IB) method<sup>28</sup> to prescribe the boundary conditions for a submerged hydrofoil. By introducing an artificial force  $\mathbf{F}_{IB}$  as a source term on the right-hand side of the momentum equation, the effect of the immersed body can be modeled. The forcing term is reconstructed according to the velocity boundary conditions and the velocity field adjacent to the body surface, and thus  $\mathbf{F}_{IB}$  should be updated in each time step. In the present IB method, the signed distance function field is used to identify the position of the body surface<sup>37</sup> implicitly. An improved moving least squares (MLS) interpolation scheme based on the signed distance function is applied to reconstruct the velocity at the forcing points with a circular supporting domain, and thus high-order interpolation can be constructed straightforwardly.<sup>28</sup>

One of the significant improvements in the present study is the use of BAMR. This allows one to faithfully track the interface and

other discontinuities with high resolution and provides savings in both the computational time needed and data storage required. The BAMR method takes the non-overlapping blocks to cover the computational domain, and all blocks are indexed by octree or quadtree data structures with the same logical configuration.<sup>29</sup> Each block is discretized by a uniform Cartesian mesh with several guard layers for enforcing boundary conditions or as the buffer layers of parallel communication, and thus it is suitable for the implementation of high-order schemes with wide stencils (e.g., WENO<sup>38</sup>). In the present BAMR method, a Peano–Hilbert space-filling curve is applied to maintain the loading balance among the multiprocessors automatically. Since the block is used as the basic manipulation unit for parallel computation, it is particularly suited to massively parallel computations. An efficient interpolation is adopted to discretize the Laplacian operator on the adaptive mesh.<sup>29</sup> Third-party mathematical libraries, including HYPRE<sup>39</sup> and PETSc,<sup>40</sup> are applied to solve the large sparse system efficiently.

### III. VALIDATION AND CONVERGENCE STUDY

For comparison, the numerical simulation is performed based on the towing tank experiment of a surface-piercing NACA 0024 foil.<sup>3</sup> In this experiment, three cases with Froude numbers  $Fr = 0.19, 0.37,$  and  $0.55$  are considered, corresponding to Reynolds numbers  $Re = 0.822, 1.52,$  and  $2.26 \times 10^6$ ; the details are summarized in Table I. The experimental measurements include mean wave elevations, unsteady near-field wave elevations, foil-surface pressures, etc.<sup>3</sup> However, the complexity of unsteady wave-induced aerated flow makes detailed experimental flow measurements very difficult.<sup>2,3</sup> Previous numerical studies<sup>11,12</sup> have revealed the flow instability mechanism and the wave-induced flow separation near the foil. However, the nature of the two-phase flow structures in the violent two-phase mixed region and the air entrainment features near foil are not fully explained. In the present work, the formation of a wedge-shaped hydraulic jump and the near-field bubbly wake are well resolved by the adaptive mesh. Therefore, instantaneous and time-averaged bubbly flow characteristics can be elucidated quantitatively.

The principal geometric parameters for NACA foil are given as chord length  $c = 1.2$  m, half-beam  $b = 0.145$  m, overall height  $D = 2$  m, and draft  $d = 1.5$  m (Fig. 2). We use the Froude number  $Fr = U/\sqrt{g\bar{c}}$  to characterize the current problem, where  $U$  is the inflow velocity and  $g$  is the gravitational acceleration. The chord length  $c$  is used to nondimensionalize the wave elevations and spatial

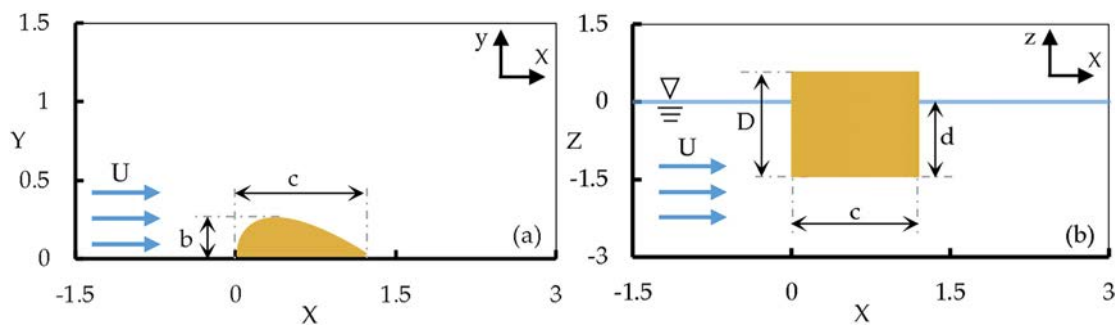


**FIG. 2.** Schematic of the computational domain: (a) top view ( $x$ – $y$  plane), (b) side view ( $x$ – $z$  plane).

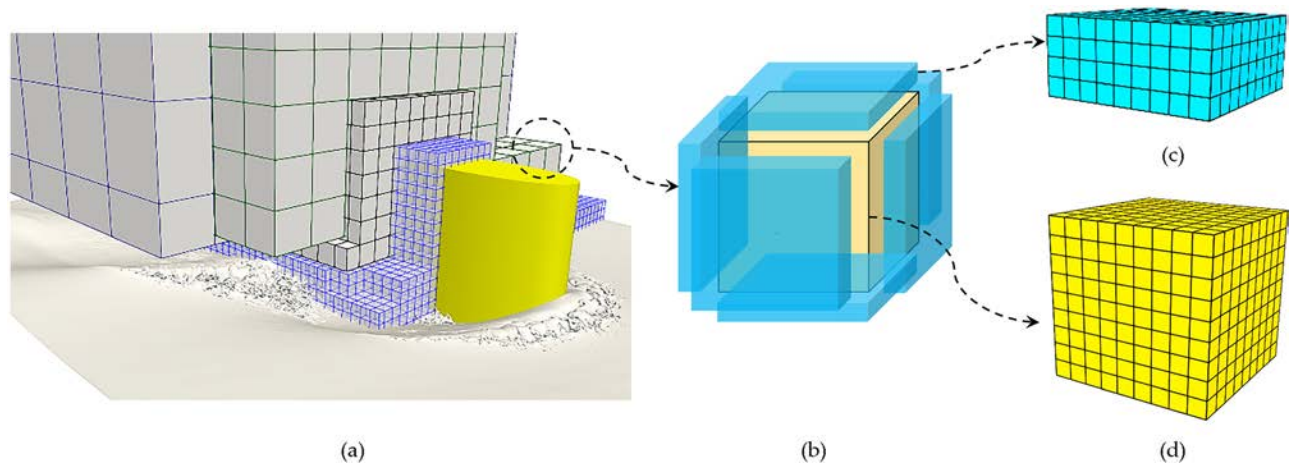


FIG. 3. (a) Schematic of BAMR blocks (refinement level 3–6); (b) grid layout of a single block; (c) guard cells (four layers); (d) Cartesian mesh ( $10 \times 10 \times 10$ ) inside a block.

coordinates for presentation. In present study, the geometrical configuration is set to satisfy the deep-draft condition as in the experiment.<sup>3</sup>

One of the main focuses of the present simulation is characterization of the main features of air-entraining turbulent hydraulic jumps, which is usually initiated near the mid-body of the model. We size the computational domain to be  $L_x = L_z = 4.5$  m in the streamwise and vertical directions and  $L_y = 1.5$  m in the spanwise direction, and thus the bow wave region and shoulder wave breaking region are well covered. The boundary conditions are as follows: a uniform inflow condition is prescribed on the inlet boundary ( $-x$  plane); the mass-conserving outflow condition is used for the right outlet boundary ( $+x$  plane) and a damping zone is adopted near the boundary to reduce the effect of wave reflection; symmetry condition and zero-gradient extrapolations of pressure and velocity field are assumed for the  $-y$  and  $+y$  planes, respectively; an impenetrable slip condition is used on the bottom ( $-z$  plane) and a constant pressure is assumed on the top boundary ( $+z$  plane).

Blocks of different refinement levels used to generate computational grids in the BAMR method are shown in Fig. 3. All blocks have a uniform grid layout with  $10 \times 10 \times 10$  computational grids [Fig. 3(d)] and four guard cells [Fig. 3(c)] for boundary treatment. Grid convergence studies are performed for  $Fr = 0.37$ . Table II summarizes the parameters for grid setup and parallel computation.

Figure 4(a) shows the general mean wave profiles adjacent to the foil with coarse, medium, and fine grids. The present numerical predictions of the bow wave envelope and the location of the jump toe

(the headmost position of a turbulent hydraulic jump) show slight discrepancies between the medium and fine grids. The small deviation downstream can be explained by intense turbulent fluctuations and droplet splashing. We present the instantaneous free surface (top view) rendered by the ray-tracing method<sup>41</sup> for the  $Fr = 0.37$  [Fig. 5(a), Multimedia view] and  $Fr = 0.55$  [Fig. 5(b), Multimedia view] cases. By using fine adaptive mesh (refinement level: 3–7), large-scale bubbles can be resolved for both cases, as shown in Figs. 5(c) and 5(d) (Multimedia view) for  $Fr = 0.37$  and  $0.55$ , respectively.

To validate the computational method and solver, the predicted near-field wave profile is compared with experimental measurements<sup>3</sup> and previous simulation results.<sup>11,12</sup> As shown in Fig. 4(b), the bow wave trough before the jump toe and the “abrupt recovery” in the hydraulic jump region are captured accurately compared with the results obtained by URANS<sup>11</sup> and detached eddy simulation (DES).<sup>12</sup> However, the wave amplitude is found to be underpredicted near the toe, with the jump toe position moving forward by 5% compared with EFD.<sup>3</sup> These discrepancies can be partly explained by the time-averaging operation for obtaining the free surface elevation, in which splashing droplets and bubbles (due to shoulder wave breaking and flow impingement) are taken into account in the violent two-phase flow mixing region.

Time-averaged wave elevation contours for  $Fr = 0.37$  are also consistent with EFD data [Fig. 4(c)]. The sharp rise of wave elevation due to the hydraulic jump is well resolved. The predicted size of the wedge-shaped region farther downstream is better than the previous CFD results.<sup>11</sup> The Kelvin wave that develops away from the NACA foil in EFD is also reproduced well.

In the turbulent hydraulic jump region, one of the important flow properties is the periodic free-surface fluctuations, which are closely related to coherent vortex shedding below the free surface.<sup>3,11,42</sup> Large fluctuations and vortex motion induce free-surface deformations and discontinuities, which will cause air entrapment underwater.<sup>27,42–47</sup> In this case, the large-scale coherent vortex motion is caused mainly by flow separation near the foil, and therefore accurate resolution of the dominant flow instabilities in the hydraulic jump region is of vital importance for the following analysis.

TABLE II. Adaptive mesh configurations for the mesh independence study.

Refinement level	Minimum grid size $\Delta$ (mm)	Total grid number	No. of processors
3–5	8	$(5.57\text{--}5.61) \times 10^6$	80
3–6	4	$(22.3\text{--}23.2) \times 10^6$	120
3–7	2	$(67.9\text{--}88.4) \times 10^6$	200

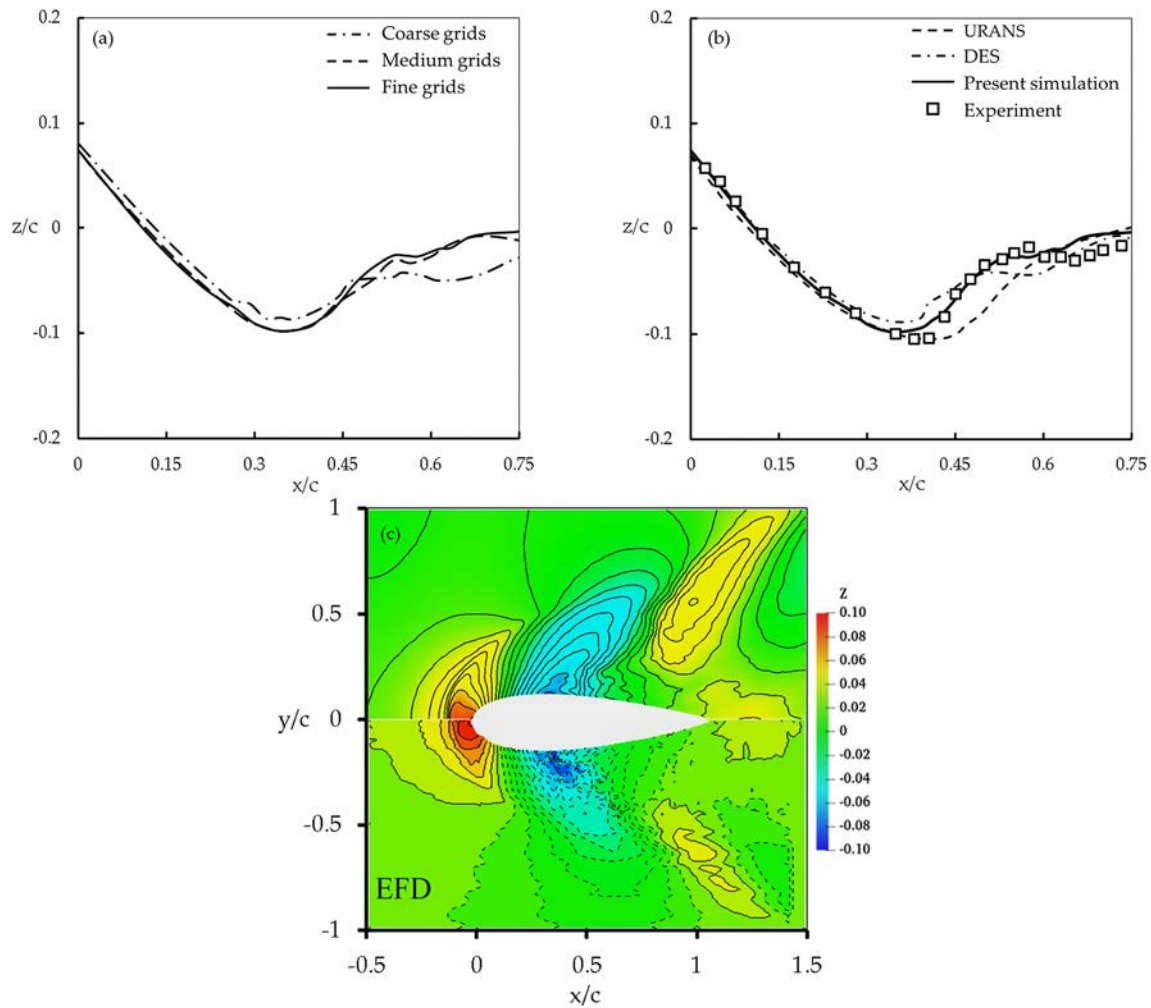


**FIG. 4.** Grid convergence study and comparison between numerical and experimental results. (a) Time-averaged wave profile with different grid resolutions for  $Fr = 0.37$ : -•-, coarse grids; - - -, medium grids; —, fine grids. (b) Quantitative comparison of the wave profile: □, experiment;<sup>3</sup> - - -, URANS;<sup>11</sup> -•-, DES;<sup>12</sup> —, present simulation. (c) Time-averaged contours of free-surface elevation ( $Fr = 0.37$ ), experimental data are extracted from Fig. 4(b) of Ref. 11.

By using the fast Fourier transform (FFT), the wave elevation spectrum and dominant periodic modes can be obtained at representative locations. In our simulation, data are sampled simultaneously at 410 Hz with a 10 s duration for each wave elevation probe, which is consistent with experimental setups.<sup>3</sup> The FFT of the wave elevation and the power spectral density (PSD) at two selected points (probe 1 at  $x/c = 0.49$  and  $y/c = 0.1275$ ; probe 2 at  $x/c = 0.8475$  and  $y/c = 0.1158$ ) are shown in Figs. 6 and 7, respectively. Two characteristic frequencies  $f_{SL} = 1.76$  Hz (Strouhal number  $St = 1.67$ ) and  $f_{KM} = 0.78$  Hz ( $St = 0.74$ ) corresponding to the shear layer instability and Kármán instability,<sup>3,11</sup> respectively, can be clearly seen, which are also consistent with experimental measurements<sup>3</sup> ( $f_{SL} = 1.73$  Hz and  $f_{KM} = 0.77$  Hz). As pointed by Kandasamy *et al.*,<sup>11</sup> shear layer instability is initiated by the separation of the shear layer near the jump toe, while the Kármán instability is associated with the reattachment of the separated vortex downstream.<sup>3,11</sup> It should be noted that the predicted FFT shows a broader band and larger amplitude of frequencies than

observed in EFD, owing to the unresolved energy loss from turbulent dissipation caused by small-scale vortex motion and splashing.<sup>12</sup> Nonetheless, the typical  $-2$  and  $-3$  power-law exponents in PSD related to turbulent dissipation near the free surface as measured in the experiment<sup>3</sup> can be predicted accurately (Fig. 7). Therefore, the results provide further validation of present solver in simulating violent free surface flows.

#### IV. CHARACTERISTICS OF HYDRAULIC JUMP AND TWO-PHASE FLOW PATTERNS

As observed in towing tank experiments,<sup>3</sup> for low- $Fr$  cases (e.g.,  $Fr = 0.19$ ), the wave profile remains in a steady state and no hydraulic jump forms near the after-body region, and only a slight variation of the wave height is found owing to the existence of a bow wave crest. As  $Fr$  increases ( $Fr \geq 0.37$ ), an abrupt change in wave elevation accompanied by shoulder wave breaking and subsequent jet splashing is observed. In this section, the formation and evolution of hydraulic

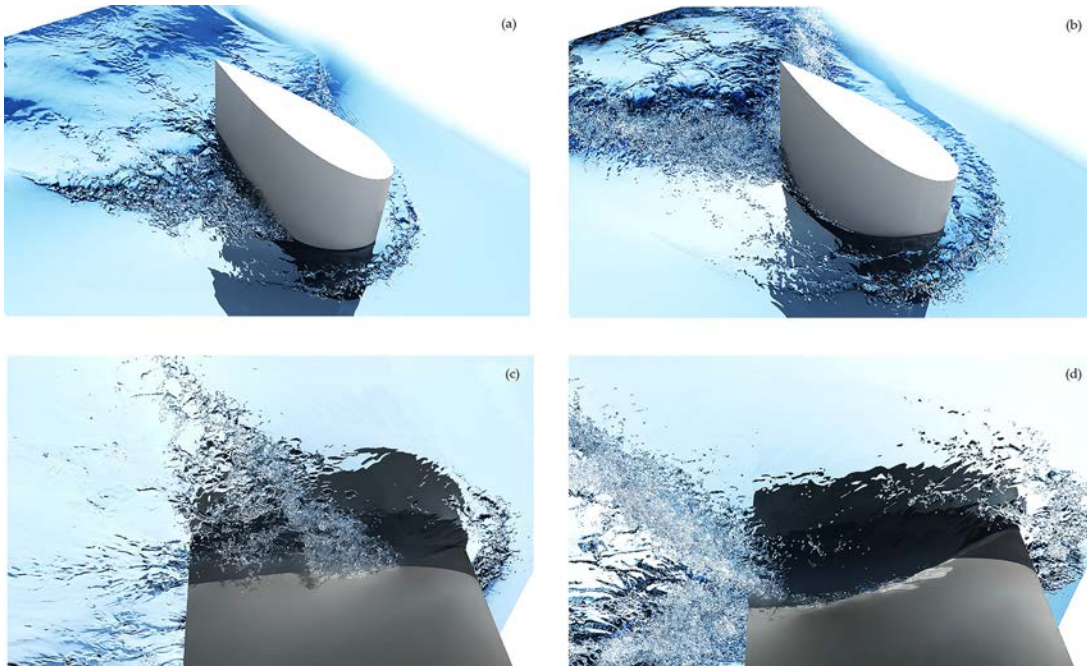


**FIG. 5.** Visualization of the predicted free surface adjacent to the NACA foil (refinement level: 3–7). (a) and (b) Top views for  $Fr = 0.37$  and  $0.55$ , respectively. (c) and (d) Underwater views of the bubbly flow for  $Fr = 0.37$  and  $0.55$ , respectively. The iso-surfaces are extracted with  $C = 0.5$  and rendered by a ray tracing toolkit.<sup>41</sup> Multimedia views: <https://doi.org/10.1063/5.0074943.1>; <https://doi.org/10.1063/5.0074943.2>; <https://doi.org/10.1063/5.0074943.3>; <https://doi.org/10.1063/5.0074943.4>.

jumps, instantaneous and average two-phase flow structures for medium and high Froude numbers ( $Fr = 0.37$  and  $0.55$ , respectively) are presented and discussed.

**A. Development of hydraulic jumps**

First, the evolution of hydraulic jumps, including the initiating mechanism, is described. Figure 8 shows the instantaneous free-surface

profile around a NACA foil for two different Froude numbers ( $Fr = 0.37$  and  $0.55$ ). For  $Fr = 0.37$ , in the initial stage, the wave runs along the vertical wall of the foil ( $t = 0.25$  s), and subsequent overturning and breakup of the bow wave generates numerous droplets ( $t = 0.75$  s). After the initial impact, the bow wave becomes mild, and reflective waves are formed by the blocking effect of the vertical foil ( $t = 1.75$  s). The wave height increases gradually with the accumulation of water in front of the foil. Eventually, a spilling breaker of the

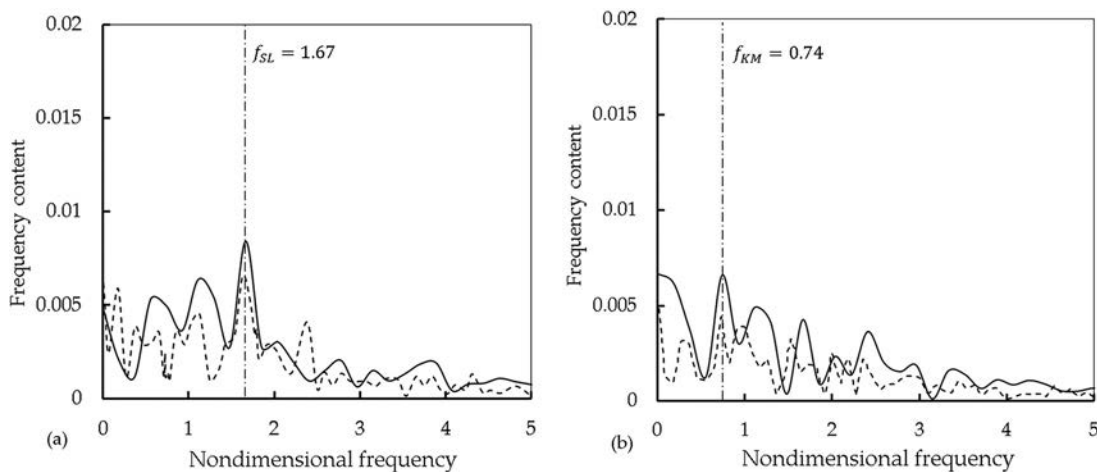


**FIG. 6.** Fast Fourier transforms of free-surface wave elevation ( $Fr = 0.37$ ): —, present simulation; - - -, experiment.<sup>3</sup> (a) FFT of the wave elevation at probe 1, with nondimensional shear layer frequency  $f_{SL} = 1.67$ ; the FFT raw signal of the experiment<sup>3</sup> is shown. (b) FFT of wave elevation at probe 2, with nondimensional Kármán frequency  $f_{KM} = 0.74$ . Experimental data are reproduced from Figs. 7(d) and 7(e) of Ref. 3 for comparison.



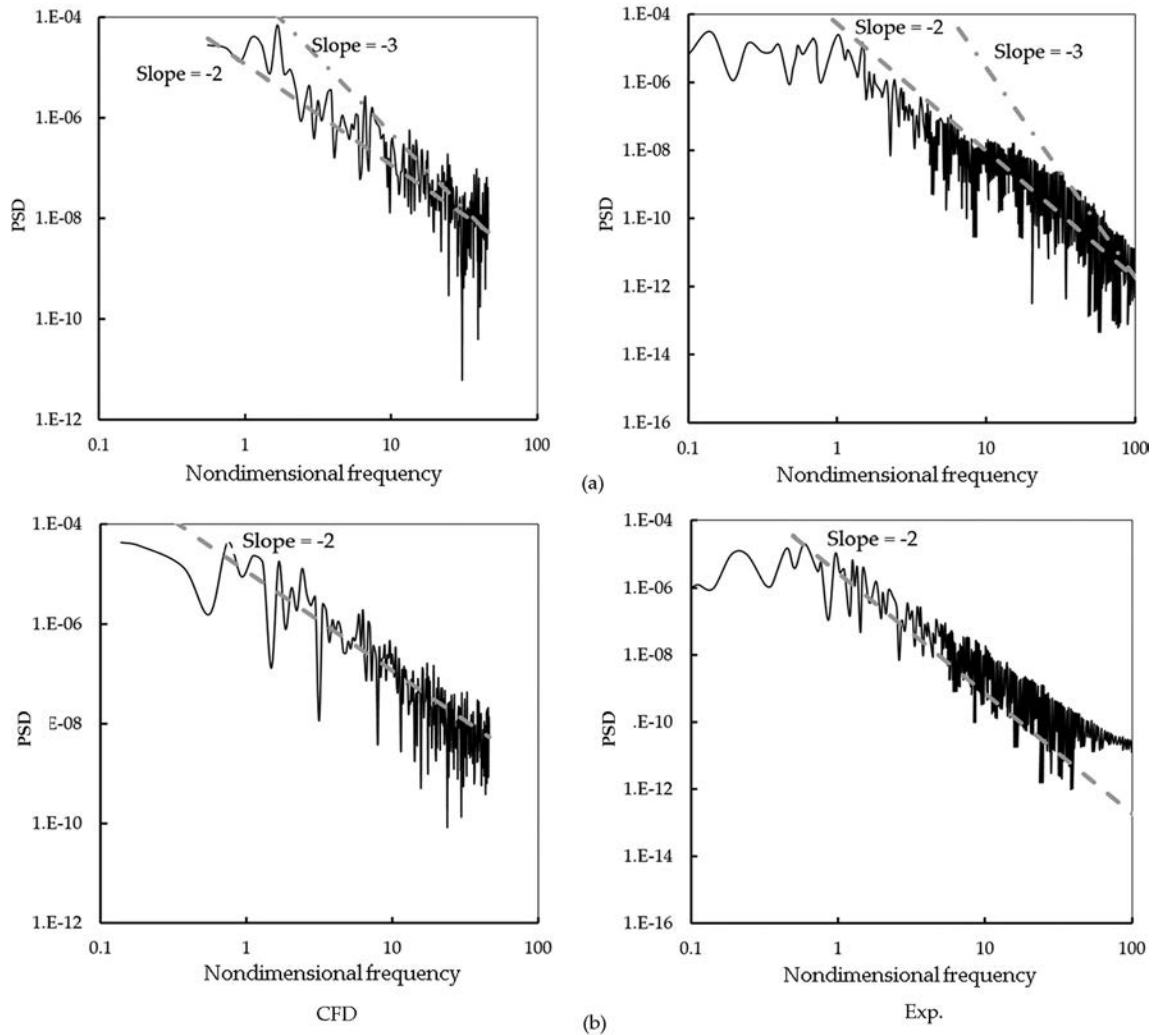


**FIG. 7.** Power-spectral densities of free-surface wave elevation ( $Fr = 0.37$ ): (a) at probe 1; (b) at probe 2. Experimental data are reproduced from Figs. 7(d) and 7(e) of Ref. 3 for comparison.

forward wave (as observed in the experiment<sup>3</sup>) appears ( $t = 2.75$  s). At the mid-waterline region around the foil, flow impinges on the model, resulting in splashing within the bow wave trough ( $t = 0.75$  s). Pogozelski *et al.*<sup>2</sup> reported that the water impingement and bow wave breaking cause considerable energy loss, which will create a significant lateral difference in total head between the flow near the model and the flow farther away from it. This difference results in flow toward the body and ever-increasing free-surface elevation near the after-body of the model. Finally, a shoulder wave, which is characterized by an abrupt change in the elevation of the wave front, is generated ( $t = 1.75$  s). The clockwise overturning of the shoulder wave and subsequent jet splashing at  $t = 1.75$  s and  $t = 2.75$  s create a discontinuity between the incoming flow and the recirculating upper flow, which can be regarded as one of the major sources for air entrainment. Finally, a steady wedge-shaped hydraulic jump with a wave-elevation difference, violent shoulder wave breaking, and air–water mixing is formed ( $t = 2.75$  s).

When  $Fr = 0.55$  [Fig. 8(b)], the initial impact becomes stronger ( $t = 0.25$  s), and this is followed by the formation of the enormous bow wave ( $t = 0.75$  s). The hydraulic jump toe is shifted toward the trailing edge by the more energetic inflow. Wave elevations increase significantly, jet impingement and splashing adjacent to the foil are more violent. Compared with the case of  $Fr = 0.37$ , a broader shoulder wave with violent breaking is observed. More droplets are generated, together with a larger amount of air being entrained underwater.

### B. Spatial patterns of wave surface

After the free-surface flow developed into a statistically steady state, we compared the predicted wave profiles in the wedge-shaped hydraulic jump region with experimental measurements. For both cases, the steady turbulent hydraulic jumps featuring violent wave breaking with jet impingement and air entrainment phenomena are

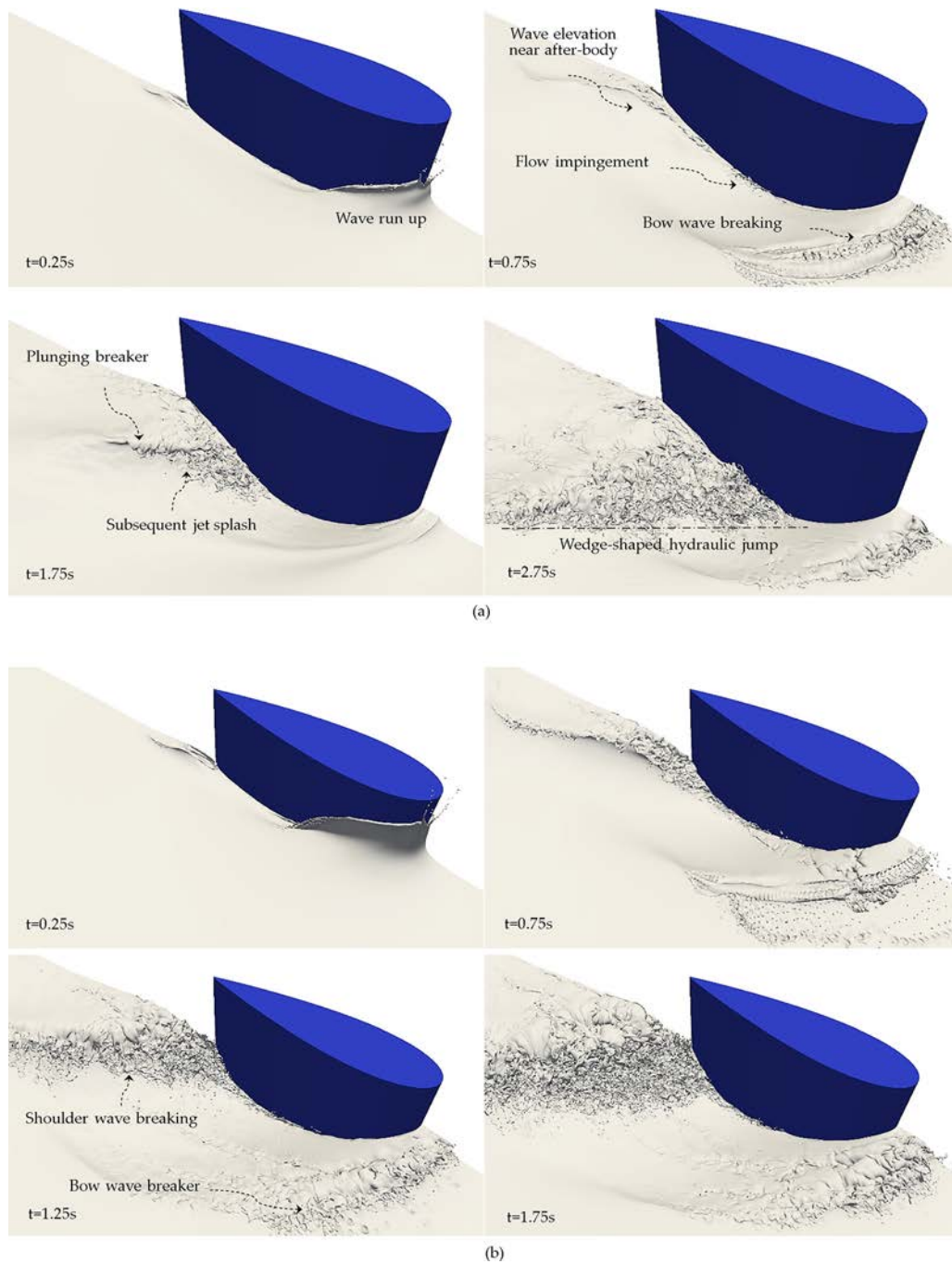


**FIG. 8.** Instantaneous free-surface evolution of a surface-piercing NACA 0024 foil: (a)  $Fr = 0.37$  and (b)  $Fr = 0.55$ .

well reproduced in our simulation [Fig. 9(b)]. In the wave trough region, intense jet splashing and pinching-off make the region laden with numerous droplets. The near-foil structures are multiscale, highly turbulent, and vigorously water–air mixed, which makes it very

difficult to discern the underlying physical mechanism. For the case of higher Froude number ( $Fr = 0.55$ ), the point of flow impingement moves to the after-body of the foil [Figs. 9(c) and 9(d)], and stronger hydraulic jumps generate more small droplets or bubbles.

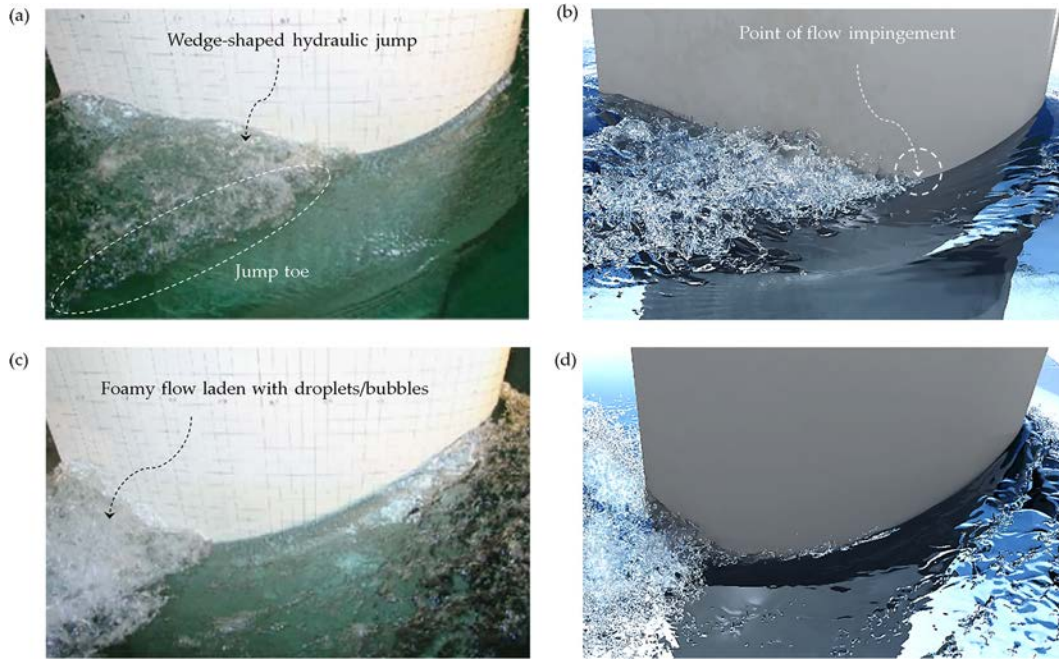


**FIG. 9.** Hydraulic jumps near the NACA 0024 foil for (a)  $Fr = 0.37$  (experimental<sup>3</sup>), (b)  $Fr = 0.37$  (present CFD), (c)  $Fr = 0.55$  (experimental<sup>3</sup>), and (d)  $Fr = 0.55$  (present CFD). (b) and (d) represent the instantaneous iso-surfaces extracted with volume fraction  $C = 0.5$ .

Three-dimensional average flow features of the two cases ( $Fr = 0.37$  and  $0.55$ ) are presented in Figs. 10 and 11 to clarify the intrinsic mechanism of hydraulic jump. Figure 10 shows the average free surface colored by velocity magnitude, and we can clearly see that both the bow wave and the hydraulic jump region contain a velocity deficit region; the former can be explained by the blocking effect of the blunt bow, while the reverse flow away from the foil surface can be attributed to shoulder wave breaking and splashing. Figure 10 indicates a strong correlation between the hydraulic jump and the velocity deficit. For both cases, the largest shear velocity appears near the

jump toe, and this induces flow separation below the free surface. The velocity deficit in the streamwise direction then makes water accumulate in the downstream region, and the bulk of the water tends to plunge and break under the effect of gravity. Finally, a wedge-shaped hydraulic jump with subsurface flow separation is formed. For the high- $Fr$  case, the subcritical flow region shifts downstream and becomes much broader with full development of the hydraulic jump.

Figure 11 depicts the average streamlines below the free surface. For both Froude numbers, shoulder wave breaking produces strong

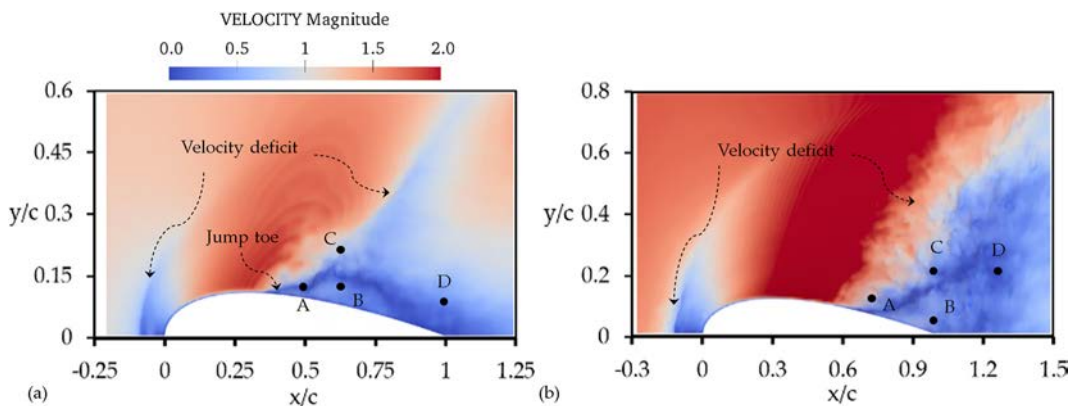


**FIG. 10.** Top view of the time-averaged free surface colored by velocity magnitude for (a)  $Fr = 0.37$  and (b)  $Fr = 0.55$ . The locations for extracting the velocity profiles are as follows: for  $Fr = 0.37$ , A,  $x/c = 0.5$ ,  $y/c = 0.125$ ; B,  $x/c = 0.62$ ,  $y/c = 0.125$ ; C,  $x/c = 0.62$ ,  $y/c = 0.2$ ; D,  $x/c = 1.0$ ,  $y/c = 0.08$ ; for  $Fr = 0.55$ , A,  $x/c = 0.62$ ,  $y/c = 0.1$ ; B,  $x/c = 1.0$ ,  $y/c = 0.042$ ; C,  $x/c = 1.0$ ,  $y/c = 0.2$ ; D,  $x/c = 1.3$ ,  $y/c = 0.2$ .

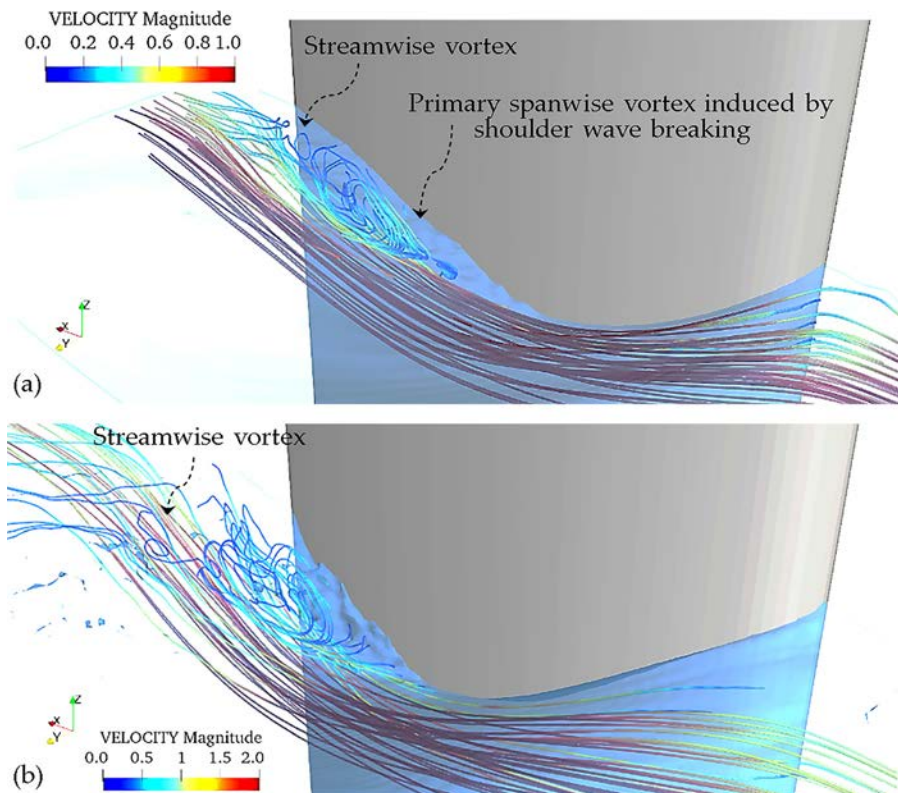


FIG. 11. Time-averaged streamlines colored by velocity magnitude together with average free surface: (a)  $Fr = 0.37$ ; (b)  $Fr = 0.55$ . The mean iso-surface is extracted with volume fraction  $\bar{C} = 0.5$ .

clockwise rollers at the intersection of the body with the water surface. The recirculating region contains large-scale turbulent rollers, which will cause considerable energy dissipation. In the region farther downstream, the counter-rotating streamwise vortex tubes originating from shoulder wave breaking detach from the body surface and generate a separated region near the trailing edge of the foil. For  $Fr = 0.55$ , the streamwise vortex tubes are convected into the wake region [Fig. 11 (b)], and flow separation near the foil is less significant. As shown in Sec. IV C, the separated flow has appreciable effects on the general distribution of two-phase flow characteristics.

**C. Two-phase mixed flow characteristics of flow field**

Wave breaking in the turbulent hydraulic jump region brings violent air–water mixing near the foil, which involves intense free surface fluctuations, spray, and air entrainment. In this work, the mixed two-phase region is represented by  $0.01 < \bar{C} < 0.99$ , where  $\bar{C}$  is the time-averaged volume fraction, which is interpolated in each cell during the simulation as

$$\bar{C}_{i,j,k} = \frac{1}{T} \int_t^{t+T} C_{i,j,k} dt. \tag{8}$$

Figure 12 shows transverse cuts (in the  $y-z$  plane) of the average velocity field at three typical positions. In the plane close to the hydraulic jump toe [ $x/c = 0.5$  and  $0.62$ , corresponding to locations A in Figs. 10(a) and 10(b), respectively], a low-speed recirculation region

appears. The backflow is partly induced by hydraulic extrusion of the advancing foil. It also leads to rising wave elevation and intensifying wave splashing adjacent to the foil, as also shown in Fig. 8. For both cases, we find that the spray region ( $0.01 \leq \bar{C} \leq 0.5$ ) containing intense bubbles and droplets experiences a sharp velocity deficit. Away from the foil, the downward motion of the fluid can be partly attributed to the development of a bow wave trough [Figs. 12(a) and 12(b)]. Farther downstream [Figs. 12(c) and 12(d)], the subcritical region with velocity deficit expands as the breaking shoulder wave shifts outward. The horizontal velocity toward the body is responsible for the continuous accumulation of water near the after-body of the foil. For  $Fr = 0.37$  specifically, the vortical flow generated by flow separation creates a downward velocity and leads to a greater depth of the mixed region ( $0.01 \leq \bar{C} \leq 0.99$ ) near the foil. Near the trailing edge [Fig. 12(e)], the shoulder wave breaking occurs far away from the foil and the upwelling flow is more prominent, with relatively constant wave elevation. For  $Fr = 0.55$ , the wave elevation grows gradually even in the wake flow region [Fig. 12(f)], with a larger two-phase mixing region. It should be noted that the upward flow in the deeper fluid imposes a vertical constraint on the mixed region, and thus bubbles cannot be entrained deeper in the wake.

For the canonical hydraulic jump [Fig. 1(b)], the averaged velocity field is basically distributed in two dimensions. The presence of the hydrofoil, however, results in apparent three-dimensional effects, with the formation of a wedge-shaped hydraulic jump. We select typical locations (Fig. 10) to reveal the features of the time-averaged velocity

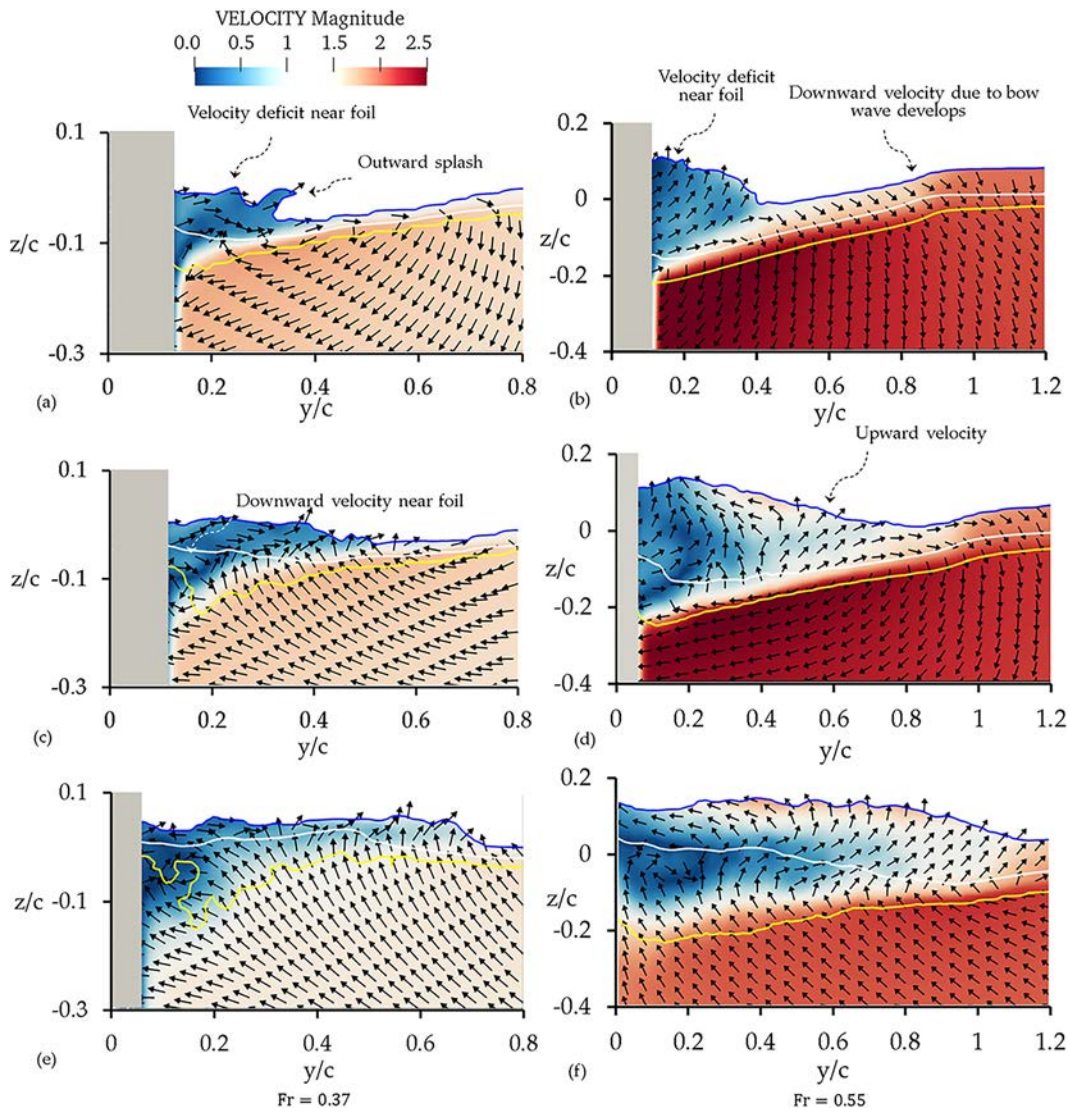


**FIG. 12.** Transverse cuts of average planar velocity: (a), (c), and (e) at  $x/c = 0.5, 0.62,$  and  $0.83$  for  $Fr = 0.37$ ; (b), (d), and (f) at  $x/c = 0.62, 0.83,$  and  $1.2$  for  $Fr = 0.55$ . White lines represent iso-contours of  $\bar{C} = 0.5$ , and the two-phase mixed region is bounded by blue lines ( $\bar{C} = 0.01$ ) and yellow lines ( $\bar{C} = 0.99$ ).

distribution, as shown in Fig. 13. When  $Fr = 0.37$ , great recirculation (near the mean interface  $\bar{C} = 0.5$ ) with a shear layer in  $\bar{u}$  appears near the foil, above the high-speed flow region. From Figs. 13(a) and 13(b), we can see that the shear flow region is not exactly in the two-phase mixing region ( $0.01 \leq \bar{C} \leq 0.99$ ). The flow separation in deeper region contributes most of the velocity shear farther downstream [Fig. 13(b)]. At locations away from the foil surface [corresponding to location C in Fig. 10(a)] that intersect the jump toe [Fig. 13(c)], the shear layer is mainly induced by the three-dimensional shoulder wave breaking, which is generally in accordance with the transition from the high-speed bulk water region to the mixed-phase region ( $0.01 < \bar{C} < 0.99$ ). There are also positive  $\bar{v}$  and  $\bar{w}$  (above the mean interface  $\bar{C} = 0.5$ ) at these locations, corresponding to the stronger outward and upward jet flow as shown

in Fig. 12(a). Besides, negative  $\bar{w}$  (below  $\bar{C} = 0.5$ ) exists near the foil surface [Figs. 13(a) and 13(b)], which can be explained by the downward vortical flow as shown in Fig. 12(c). In the wake region near the trailing edge [Fig. 13(d)], the recirculating flow in the upper fluid is no longer present, and the shear layer in the mixed-phase region recedes.  $\bar{v}$  and  $\bar{w}$  are dissipated, with minor fluctuations caused by turbulence.

For the case of  $Fr = 0.55$ , a similar velocity shear also appears in the wake region behind the foil [Fig. 13(h)], and the recirculating flow region expands as expected [Figs. 13(e) and 13(f)]. Unlike the  $Fr = 0.37$  case, the shear layer caused by flow separation in deeper flow is less easily distinguishable. As the turbulent jump toe shifts downstream in this case, we can expect a continuous increase in wave elevation from the  $\bar{w}$  profiles [Figs. 13(f)–13(h)].

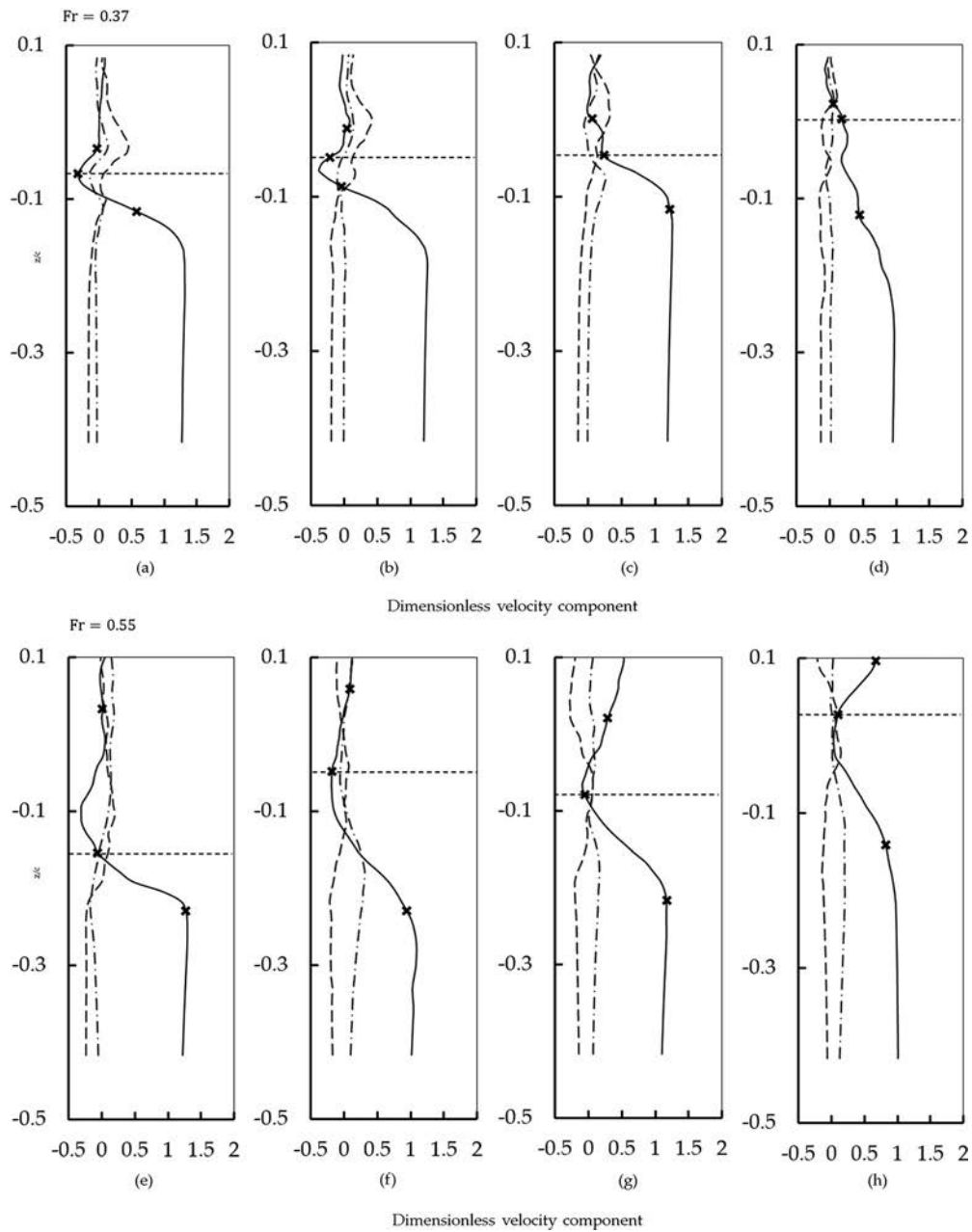


**FIG. 13.** Velocity profiles along the vertical direction at select locations: ---, positions of  $\bar{C} = 0.5$ ; —,  $\bar{u}$ ; ---,  $\bar{v}$ ; - • -,  $\bar{w}$ ; ×,  $\bar{C} = 0.01, 0.5, \text{ and } 0.99$ . Velocity components are nondimensionalized by the inflow velocity for each case. (a)–(d) and (e)–(h) correspond to locations A–D in Fig. 10 for  $Fr = 0.37$  and  $0.55$ , respectively.

The above analysis shows that the major difference between a wedge-shaped hydraulic jump and the canonical hydraulic jump arises from the three-dimensional effect, which is caused by the shoulder wave breaking and resultant flow separation below the free surface. Therefore, the flow physics near the wall boundary becomes more complex and alters the internal mixed flow patterns. Also, it is found that the three-dimensional wave breaking is highly correlated with the

large-scale air entrainment behavior near the foil. We will illustrate this further in Sec. V.

### V. FEATURES OF AIR ENTRAINMENT

This section aims to determine the characteristics of large-scale air entrainment using a bubble/droplet detection program and to provide a physical understanding of air entrainment near the surface-

piercing NACA foil. Generally speaking, the air entrainment is mainly due to shoulder wave breaking. Usually, large air pockets are entrapped into the water when the plunging jet contacts the wave trough. Air pockets quickly breakup into large bubbles when turbulent shear stress overcomes the stabilizing surface tension force. Small bubbles are formed by the cascade breakup of large bubbles as they are transported downstream. Far away from the foil, the air entrainment process in the hydraulic jump region is similar to plunging wave breaking, in both scenarios, the overturning jet flow impinging wave surface with the entrapment of large air pockets can be observed. Although the plunging wave patterns and the general air entrapment properties have been well understood by experimental studies,<sup>15,16,48–51</sup> the differences between the canonical wave breaker and the hydraulic jump induced breaking waves need to be clarified. Besides, it is difficult to perform quantitative analysis for the unsteady air entrapping process by experiment. With the high-fidelity numerical simulation, large-scale bubbles are resolved thus the main features of bubble cloud can be obtained, e.g., the evolution of the entrapped air cavity, the spatial distribution of the bubble clouds, and the bubble size spectrum etc.

**A. Evolution and distribution of entrapped air**

For both cases, the temporal evolution of the entrapped air volume exhibits three typical stages (Fig. 14), which can be characterized

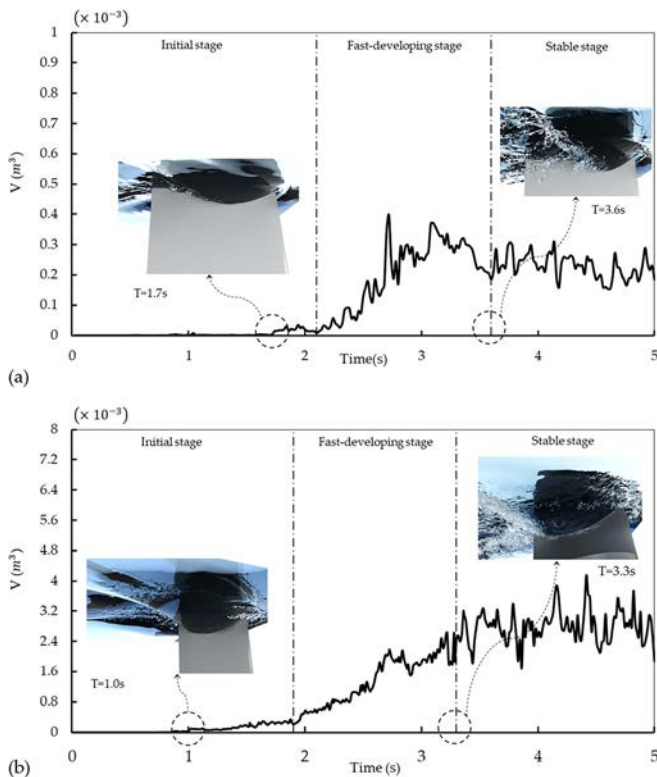


**FIG. 14.** Entrapped bubble volume vs time with the snapshots of air entrainment in the hydraulic jump region at specific instants for (a)  $Fr = 0.37$  and (b)  $Fr = 0.55$ .

by different air entrainment rates. In the initial stage, the bow wave generated by the initial impact quickly breaks up into thin liquid filaments and microdroplets, and a minimal amount of air is entrapped into the water as the liquid filaments or droplets impact on the free surface. When the turbulent hydraulic jump is initiated and accompanying shoulder wave breaking occurs, a large bulk of air will be engulfed by the overturning wave front, and thus the volume of air entrainment increases dramatically. The violent water–air interactions and chaotic changes in the free surface near the toe make the signal noisy. In the stable stage, the total volume of submerged air attains a stable oscillation state. Large-scale air pockets breakup into smaller-scale bubbles under strong turbulent shear, creating a bubble cloud near the jump toe. The bubble cloud in this area is transported downstream and diffused into the wedge-shaped region.

Specifically, we find that the total air volume shows a sharp decrease for lower Froude numbers ( $Fr = 0.37$ ). With the full development of the hydraulic jump, a plunging breaker of the shoulder wave occurs far away from the foil. Subsequent jet impingement becomes the dominant factor and is also responsible for air entrainment, and although this process entraps many more microbubbles into the water, the total entrained air volume is relatively small. Larger bubbles driven by buoyance may escape from the free surface quickly in the fast-developing stage, resulting in an appreciable loss of entrained air volume.

Figure 15 presents the time-averaged void fraction contour at the cross sections of  $x/c = 0.4, 0.65, 0.9,$  and  $1.15$  for  $Fr = 0.37$  and  $0.55$ . It is found that the occurrence of air entrainment corresponds to the wedge-shaped hydraulic jump region, while the bubble cloud transported from upstream can be more clearly identified in the high- $Fr$  case [Fig. 15(b)] owing to enhanced bow wave breaking. For both cases, the bubble cloud is generated near the jump toe and transported away from the model farther downstream. When  $Fr = 0.37$ , the bubble cloud separates into two parts (Regions 1 and 2) in the after-body region. Region 1 is near the location at which the shoulder wave breaks away from the foil surface. In this region, bubbles mostly cluster near the free surface as the upward flow induced by the hydraulic jump prevents them from transporting deeper, as illustrated in Figs. 12(c) and 12(e). Region 2 corresponds to the flow separation region, in which the bubble cloud has a greater penetration depth. Similar to the experimental observation,<sup>2</sup> smaller bubbles can be easily trapped by a strong vortex near the foil and entrained in the deeper fluid. The downward flow caused by flow separation is clearly revealed by the velocity vectors in Fig. 12(c) and the vertical velocity component  $\bar{w}$  in Fig. 13(b). For  $Fr = 0.55$ , the bubble cloud has a relatively uniform penetration depth along the spanwise direction as the flow separation develops into the far wake flow and large swirling motion near the foil is suppressed. The greatest penetration depths of air entrainment are  $-0.19 < z/c < -0.15$  and  $-0.24 < z/c < -0.18$  for  $Fr = 0.37$  and  $0.55$ , respectively.

The entire domain is divided into several sections to obtain the time-averaged entrained air volume [Fig. 16(a)] and surface entrainment rate [Fig. 16(b)],

$$v_b = \sum C_{i,j,k} dx dy dz, \tag{9}$$

$$\overline{V_{x_1 < x/c < x_2}} = \frac{1}{T} \int_t^{t+T} \sum v_b dt, \tag{10}$$

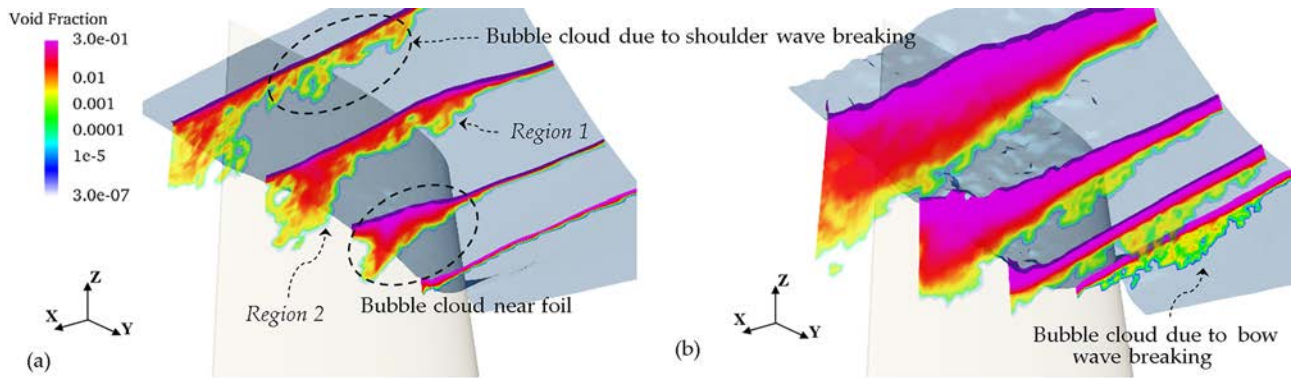


FIG. 15. Distribution of time-averaged void fraction in different cross sections: underwater views for (a)  $Fr = 0.37$  and (b)  $Fr = 0.55$ . The transparent isosurface indicates the average free surface of  $\bar{C} = 0.5$ .

$$\bar{S} = U \frac{d\bar{V}}{dx}, \tag{11}$$

where  $v_b$  is the volume of each cavity located in  $x_1 < x/c < x_2$  during the sampling time  $T$ . The average surface entrainment rate  $\bar{S}$  that represents the rate of total air entrainment through the interface is estimated by making a simplified mass conservation argument in an infinitesimal streamwise control volume.<sup>21</sup> The initial peak of air volume occurs at  $x/c \approx 0$  owing to bow wave breaking. Farther downstream, the air entrainment increases dramatically in the hydraulic jump region as a result of the shoulder wave breaking. As expected, the breaking hydraulic jump accounts for most of the entrained air (95% of total air for  $Fr = 0.37$  and 89% for  $Fr = 0.55$ , as shown in Table III). The general trend of air volume distribution is similar for the two cases. When  $Fr = 0.55$ , the entrapped air volume  $\bar{V}$  is also appreciable in the near-field wake flow ( $1.6 < x/c < 2$ ), while it is much lower for  $Fr = 0.37$  since the bubbles appearing in this area have mostly escaped through the free surface.

Figure 16(b) shows the surface entrainment rate as a function of  $x/c$ . An initial peak  $\tilde{x}_1$  is seen in front of the bow  $x/c = -0.083$ , the secondary peak  $\tilde{x}_2$  is in the hydraulic jump region when  $x/c = 0.61$  for  $Fr = 0.37$ . Table III summarizes these locations and the corresponding  $\bar{S}$ . The two peaks of  $\bar{S}$  for  $Fr = 0.55$  are nearly twice those for  $Fr = 0.37$ . The point at which the shoulder wave forms and begins to break can be identified by the increase in surface entrainment rate. The position and amplitude of the secondary peak both have a strong positive correlation with inflow velocity. As the Froude number increases, air entrainment is significantly enhanced, especially in the hydraulic jump region. For both cases, the secondary peaks are followed by a sharp decrease, with negative  $\bar{S}$  near the trailing edge of the foil (for  $Fr = 0.37$ ) and in the wake flow region (for  $Fr = 0.55$ ).

### B. Spatial distribution and size spectrum of bubbles/droplets

We have adopted a Lagrangian description of the bubble cloud using a bubble/droplet detection algorithm similar to that of Chan

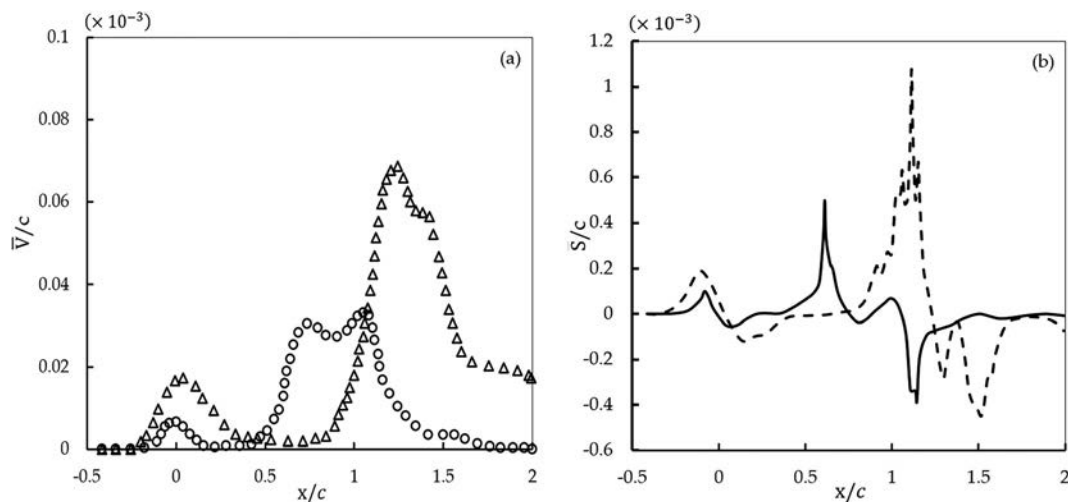


FIG. 16. (a) Time-averaged entrained air volume along the streamwise direction:  $\circ$ ,  $Fr = 0.37$ ;  $\triangle$ ,  $Fr = 0.55$ . (b) Average surface entrainment rate: —,  $Fr = 0.37$ ; - - -,  $Fr = 0.55$ .



TABLE III. Average air entrainment characteristics.

Case	$\tilde{x}_1$	$\overline{S}(\tilde{x}_1)/c$	$\tilde{x}_2$	$\overline{S}(\tilde{x}_2)/c$	Proportion of entrained air in hydraulic jump region
A2	-0.083	$0.10 \times 10^{-3}$	0.61	$0.5 \times 10^{-3}$	95%
A3	-0.099	$0.19 \times 10^{-3}$	1.11	$1.08 \times 10^{-3}$	89%

et al.<sup>50</sup> In the algorithm, each air cavity or liquid bulk is isolated from the connected free surface and labeled. The individual volume and equivalent spherical radius are calculated by

$$r_{\text{eff}} = \left( \frac{3v_b}{4\pi} \right)^{1/3}, \quad (12)$$

where  $v_b$  and  $r_{\text{eff}}$  are the volume and equivalent spherical radius of each bubble (or droplet).

Figure 17 presents the spatial distributions of the bubble clouds for two Froude numbers in the  $x$ - $y$  and  $x$ - $z$  planes. Generally, the bubble clouds are mostly distributed in two distinct regions, namely, the bow wave and the turbulent hydraulic jump, which is consistent with the distribution of entrained air volume in Fig. 16(a). There are two bands of bubble cloud near the bow for  $Fr = 0.55$  [Fig. 17(b)] owing to the spilling breaker of the bow wave and subsequent jet impacts. Bubbles generated near the bow travel with the high-speed flow below and amalgamate into the bubble cloud downstream. In the hydraulic jump region, it can be observed that the violent secondary jet splashing for the high- $Fr$  case generates many more small bubbles near the jump toe. The spread range of the bubble cloud is broader and the wake flow behind the foil contains a considerable number of bubbles of various sizes [Fig. 17(b)], whereas for  $Fr = 0.37$ , most of the larger-scale bubbles are distributed near the after-body region of the foil [Fig. 17(a)]. Moreover, numerical results show that the spread angle of the bubble cloud has no significant correlation with the inflow velocities (Froude numbers). We measure this angle by a linear fit and find that the predicted angles ( $\theta_A = 38.72^\circ$  for  $Fr = 0.37$  and  $\theta_B = 38.27^\circ$  for  $Fr = 0.55$ ) are very close to the shoulder wave envelope ( $35^\circ$ - $40^\circ$ ) measured experimentally.<sup>3</sup>

To determine the size spectrum of the bubble cloud  $\overline{N}(r_{\text{eff}}, b)$ , we count the number of bubbles within each equivalent spherical-radius bin  $n(r_{\text{eff}}, b)$  and calculate the time-averaged bubble size spectrum by

$$\overline{N}(r_{\text{eff}}, b) = \frac{1}{T} \int_t^{t+T} \frac{n(r_{\text{eff}}, b)}{b} dt, \quad (13)$$

where the bin width  $b$  is selected as 0.3 mm. The bubble/droplet size spectrum  $\overline{N}(r_{\text{eff}}, b)$  for different Froude numbers is given in Fig. 18. Dimensional analysis has shown that the droplet or bubble size distribution agree with a power-law scaling,<sup>52,53</sup> and this has been validated by several experiments.<sup>53-58</sup>

In the present simulation, the time-averaged droplet size distribution is close to  $-4.5$  power law [Fig. 18(a)], which conforms to experimental measurements<sup>57</sup> and high-fidelity simulations of spraying droplets generated by wave breaking.<sup>15</sup> It should be noted that droplets/bubbles of size smaller than  $1.5\Delta$  (where  $\Delta$  is the minimal grid size corresponding to the refinement level 3-7 in Table I) cannot be captured well, and so the unphysical decrease in density in Fig. 18 for small droplets/bubbles is less credible.

Figure 18(b) presents time-averaged bubble size distributions. For bubbles with  $R \geq 3$  mm, the power-law exponent  $\beta$  of the size spectrum is generally close to  $-10/3$ , as measured in experiments on wave breaking.<sup>53</sup> This proves that the quasi-steady turbulent breakup cascade is predominant for the bubbles identified in the present simulation. Nonetheless, the presence of a semi-submerged foil causes a slight deviation of the size distribution from the canonical  $-10/3$  to  $-4.46$  ( $Fr = 0.55$ ) and  $-4.28$  ( $Fr = 0.37$ ) power laws for larger

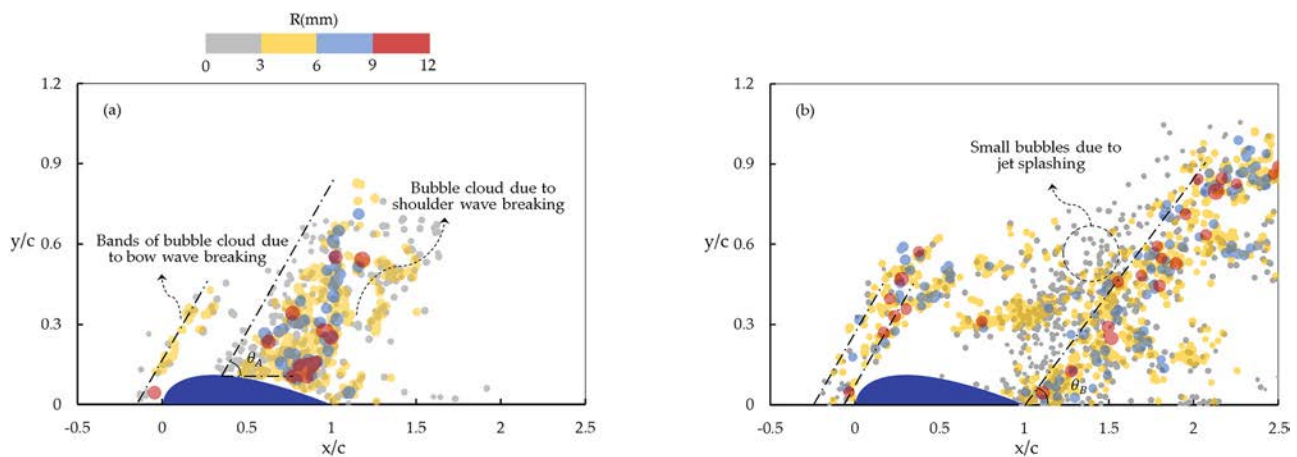
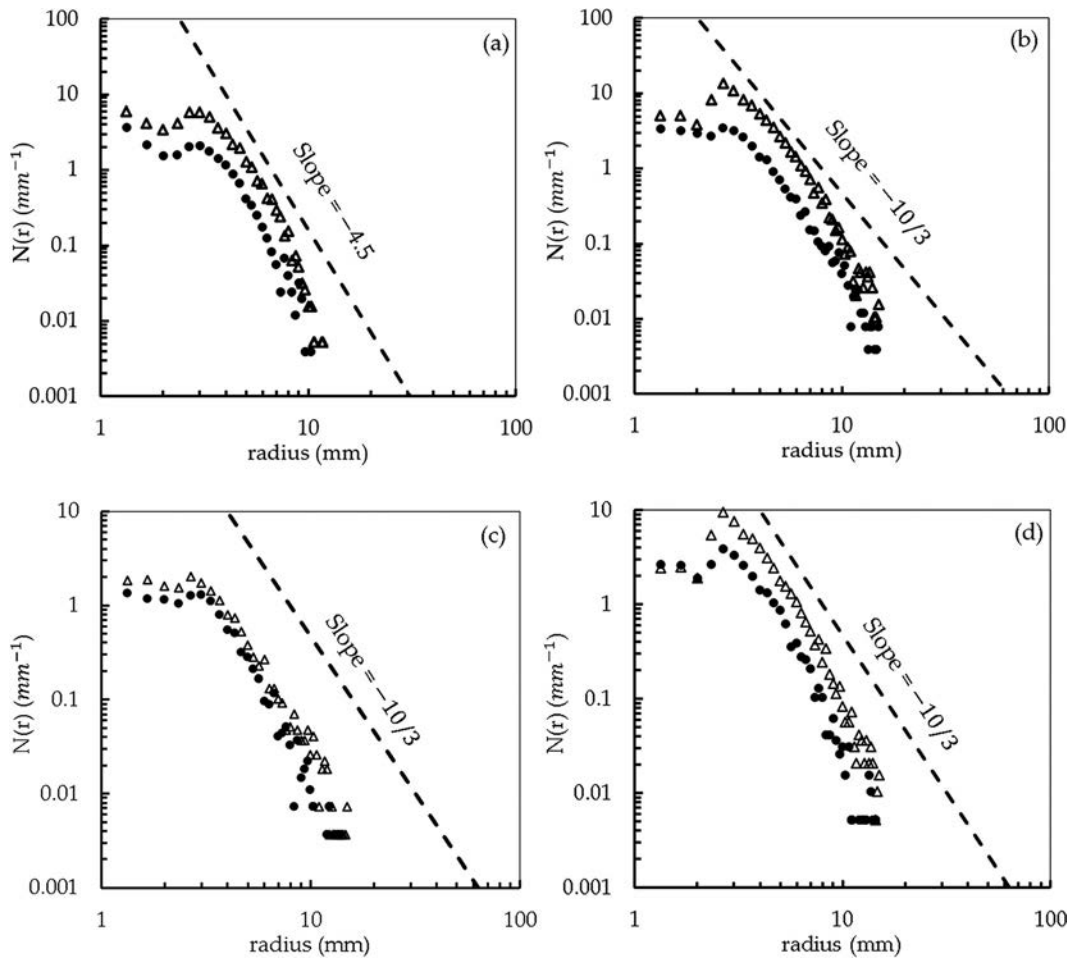


FIG. 17. Spatial distribution of multiscale entrapped bubbles with equivalent radius  $r_{\text{eff}}$  for (a)  $Fr = 0.37$  and (b)  $Fr = 0.55$ .



**FIG. 18.** (a) and (b) Total size spectra of droplets and bubbles, respectively: ●,  $Fr = 0.37$ ; △,  $Fr = 0.55$ . (c) and (d) Bubble size spectra in subregions for  $Fr = 0.37$  and  $0.55$ , respectively: ●,  $y < 2b$ ; △,  $y > 2b$ .  $N(r)$  is nondimensionalized by the total volume of the computational domain.

bubbles ( $R > 7$  mm). This deviation can be explained partly by the large-scale swirling motions of flow separation and buoyancy effects in the wake flow. The violent interactions between the strongly turbulent shear flow and bubbles lead to more fragmentation of larger bubbles. On the other hand, in the downstream region, larger bubbles in the wake flow usually rise quickly, allowing them to escape more easily from passive transport<sup>42</sup> and eventually merge with the free surface. A similar size distribution (with a mean value of  $-4.51$  for  $\beta$ ) has also been reported in the high-fidelity simulation of the bubbly wake behind a three-dimensional dry transom stern,<sup>21</sup> in which the far-field divergent wave breaking has a close resemblance to the shoulder wave breaking in the present work.

As illustrated in Fig. 17, the bubble cloud is prone to clustering near the after-body region of the foil. To investigate the dependence of the size spectrum on the spanwise distribution in  $y$ , we have separated the hydraulic jump region into two subregions. For  $Fr = 0.37$ , it is found that the regions  $y < 2b$  and  $y > 2b$  contribute almost equally to the total spectrum, as shown in Fig. 18(c) (where  $b = 0.145$  m is the half-beam of the foil), whereas for  $Fr = 0.55$ , a greater number of

smaller bubbles are generated as a result of the subsequent violent jet splashing for  $y > 2b$  [Fig. 18(d)].

### VI. SUMMARY

In this paper, high-fidelity simulations of the free surface flow around a surface-piercing NACA foil have been performed with a self-developed two-phase flow solver BAMR-SJTU. The present solver was developed based on a block-structured adaptive mesh, which is suitable for the implementation of high-resolution schemes and is highly applicable to massively parallel computations. Numerical validations show that the predicted time-averaged wave profile and wave elevation spectrum are consistent with corresponding experimental measurements.<sup>3</sup>

The analysis of air entrainment utilizes a newly developed bubble/droplet detection algorithm, originating from the processing techniques of Chan *et al.*<sup>50</sup> After post-processing, the characteristic parameters (e.g., the bubble/droplet size spectrum) of the hydraulic jump predicted by the present simulation show good agreement with related experimental data. The present study has focused on the wave

breaking pattern and large-scale air entrainment features of the hydraulic jump phenomenon, which are difficult to measure experimentally. The following conclusions can be drawn:

1. A wedged-shaped hydraulic jump is generated at the intersection of a surface-piercing foil with the free surface at relatively high Froude numbers. We find that the turbulent hydraulic jump is characterized by shoulder wave breaking and subsurface flow separation, which is different from the canonical hydraulic jump.
2. The clockwise overturning breakup of the shoulder wave and subsequent jet splashing create discontinuities between the high-speed incoming flow and the recirculating upper flow, which is a source of large-scale air entrainment.
3. Investigation of the mean flow structures in the two-phase mixed region shows that the main similarities with the canonical hydraulic jump lie in the presence of a shear layer and of recirculating flow near the foil. In the after-body region near the foil, flow separation contributes more to the generation of the shear layer, while farther away from foil, the breaking shoulder wave introduces strong three-dimensional flow structures similar to a plunging wave breaker, which also greatly enhance the air entrainment.
4. As the Froude number increases, the shoulder wave moves downstream and becomes broader. Consequently, the bubble clouds are distributed mostly in the near-field wake flow region. However, the shoulder wave pattern seems to be independent of Froude numbers. The spread angles of the bubble cloud near the jump toe for different Froude numbers are almost the same, close to the wave envelope ( $35^\circ$ – $40^\circ$ ) measured experimentally.<sup>3</sup>
5. Quantitative analysis shows that the air entrainment corresponds mainly to the turbulent hydraulic jump region. The high-Fr case produces a larger total volume of entrained air and a higher surface entrainment rate owing to the violent shoulder wave breaking process.
6. The scaled bubble size distribution shows a good match with a  $-10/3$  power law for smaller bubbles of radius  $1.5\Delta \leq R \leq 7$  mm (where  $\Delta = 2$  mm is the minimal grid interval), while there is a deviation for bubbles with  $R > 7$  mm. This deviation may be correlated with anisotropy caused by the turbulent shear flow near the foil and the buoyancy effects in the wake.

With the use of state-of-the-art numerical techniques, this work provides new insights into the violent two-phase mixed flow near a surface-piercing NACA foil. Through the present high-fidelity simulations, we have established a quantitative understanding of the flow structures and large-scale air entrainment characteristics of a breaking hydraulic jump.

## ACKNOWLEDGMENTS

This work is supported by the National Natural Science Foundation of China (11902199 and 51979160), the Shanghai Pujiang Talent Program (19PJ1406100), and the National Key Research and Development Program of China (2019YFB1704204 and 2019YFC0312400), to which the authors are most grateful.

## AUTHOR DECLARATIONS

### Conflict of Interest

The authors have no conflicts to disclose.

## DATA AVAILABILITY

The data that support the findings of this study are available from the corresponding author upon reasonable request.

## REFERENCES

- <sup>1</sup>M. Xiang, S. C. P. Cheung, J. Y. Tu *et al.*, “A multi-fluid modelling approach for the air entrainment and internal bubbly flow region in hydraulic jumps,” *Ocean Eng.* **91**, 51–63 (2014).
- <sup>2</sup>E. Pogozelski, J. Katz, and T. Huang, “The flow structure around a surface piercing strut,” *Phys. Fluids* **9**, 1387–1399 (1997).
- <sup>3</sup>B. Metcalf, J. Longo, S. Ghosh *et al.*, “Unsteady free-surface wave-induced boundary-layer separation for a surface-piercing NACA 0024 foil: Towing tank experiments,” *J. Fluids Struct.* **22**, 77–98 (2006).
- <sup>4</sup>C. Lin, S.-C. Hsieh, I.-J. Lin *et al.*, “Flow property and self-similarity in steady hydraulic jumps,” *Exp. Fluids* **53**, 1591–1616 (2012).
- <sup>5</sup>Y. Chachereau and H. Chanson, “Free-surface turbulent fluctuations and air-water flow measurements in hydraulics jumps with small inflow Froude numbers,” School of Civil Engineering, University of Queensland, Hydraulic Model Report No. CH78/10, 2010.
- <sup>6</sup>H. Chanson, “Current knowledge in hydraulic jumps and related phenomena. A survey of experimental results,” *Eur. J. Mech. B. Fluids* **28**, 191–210 (2009).
- <sup>7</sup>J. Rodríguez-Rodríguez, C. Marugán-Cruz, A. Aliseda *et al.*, “Dynamics of large turbulent structures in a steady breaker,” *Exp. Therm. Fluid Sci.* **35**, 301–310 (2011).
- <sup>8</sup>S. Misra, J. Kirby, M. Brocchini *et al.*, “The mean and turbulent flow structure of a weak hydraulic jump,” *Phys. Fluids* **20**, 035106 (2008).
- <sup>9</sup>S. Chow, “Free-surface effects on boundary layer separation on vertical struts,” Doctoral dissertation (University of Iowa, 1968).
- <sup>10</sup>F. Stern, W. Hwang, and S. Jaw, “Effects of waves on the boundary layer of a surface-piercing flat plate: Experiment and theory,” *J. Ship Res.* **33**, 63–80 (1989).
- <sup>11</sup>M. Kandasamy, T. Xing, and F. Stern, “Unsteady free surface wave-induced separation: Vortical structures and instabilities,” *J. Fluids Struct.* **25**, 343–363 (2009).
- <sup>12</sup>T. Xing, M. Kandasamy, and F. Stern, “Unsteady free-surface wave-induced separation: Analysis of turbulent structures using detached eddy simulation and single-phase level set,” *J. Turbul.* **8**, N44 (2007).
- <sup>13</sup>Z. C. Fang, L. F. Xiao, H. D. Wei *et al.*, “Severe wave run-ups on fixed surface-piercing square column under focused waves,” *Phys. Fluids* **32**, 063308 (2020).
- <sup>14</sup>M. Mortazavi, V. Le Chenadec, P. Moin *et al.*, “Direct numerical simulation of a turbulent hydraulic jump: Turbulence statistics and air entrainment,” *J. Fluid Mech.* **797**, 60–94 (2016).
- <sup>15</sup>Z. Y. Wang, J. M. Yang, and F. Stern, “High-fidelity simulations of bubble, droplet and spray formation in breaking waves,” *J. Fluid Mech.* **792**, 307–327 (2016).
- <sup>16</sup>L. Deike, W. K. Melville, and S. Popinet, “Air entrainment and bubble statistics in breaking waves,” *J. Fluid Mech.* **801**, 91–129 (2016).
- <sup>17</sup>P. Lubin and S. Glockner, “Numerical simulations of three-dimensional plunging breaking waves: Generation and evolution of aerated vortex filaments,” *J. Fluid Mech.* **767**, 364–393 (2015).
- <sup>18</sup>C. Y. Song and A. I. Sirviente, “A numerical study of breaking waves,” *Phys. Fluids* **16**, 2649–2667 (2004).
- <sup>19</sup>G. Chen, C. Kharif, S. Zaleski *et al.*, “Two-dimensional Navier–Stokes simulation of breaking waves,” *Phys. Fluids* **11**, 121–133 (1999).
- <sup>20</sup>P. Adams, K. George, M. Stephens *et al.*, “A numerical simulation of a plunging breaking wave,” *Phys. Fluids* **22**, 091111 (2010).
- <sup>21</sup>K. Hendrickson, G. D. Weymouth, X. Yu, and D. K.-P. Yue, “Wake behind a three-dimensional dry transom stern. Part 1. Flow structure and large-scale air entrainment,” *J. Fluid Mech.* **875**, 854–883 (2019).
- <sup>22</sup>K. Hendrickson and D. K.-P. Yue, “Wake behind a three-dimensional dry transom stern. Part 2. Analysis and modelling of incompressible highly variable density turbulence,” *J. Fluid Mech.* **875**, 884–913 (2019).
- <sup>23</sup>P. Peltonen, P. Kanninen, E. Laurila *et al.*, “Scaling effects on the free surface backward facing step flow,” *Phys. Fluids* **33**, 042106 (2021).

- <sup>24</sup>C. Liu, Y. Hu, Z. Li *et al.*, “Recent advancement of experimental and numerical investigations for breaking waves,” *J. Harbin Inst. Technol. (New Ser.)* **26**(5), 1–16 (2019).
- <sup>25</sup>P. Perlin and W. W. Schultz, “Capillary effects on surface waves,” *Annu. Rev. Fluid Mech.* **32**, 241–274 (2000).
- <sup>26</sup>R. Jahanbakhshi, “Mechanisms of entrainment in a turbulent boundary layer,” *Phys. Fluids* **33**, 035105 (2021).
- <sup>27</sup>R. Kelly, D. B. Goldstein, S. Suryanarayanan *et al.*, “The nature of bubble entrapment in a Lamb–Oseen vortex,” *Phys. Fluids* **33**, 061702 (2021).
- <sup>28</sup>C. Liu and C. H. Hu, “Block-based adaptive mesh refinement for fluid–structure interactions in incompressible flows,” *Comput. Phys. Commun.* **232**, 104–123 (2018).
- <sup>29</sup>C. Liu and C. H. Hu, “An adaptive multi-moment FVM approach for incompressible flows,” *J. Comput. Phys.* **359**, 239–262 (2018).
- <sup>30</sup>X. B. Yang, C. Liu, D. C. Wan, and C. H. Hu, “Numerical study of the shock wave and pressure induced by single bubble collapse near planar solid wall,” *Phys. Fluids* **33**, 073311 (2021).
- <sup>31</sup>M. Sussman and E. G. Puckett, “A coupled level set and volume-of-fluid method for computing 3D and axisymmetric incompressible two-phase flows,” *J. Comput. Phys.* **162**, 301–337 (2000).
- <sup>32</sup>S. Ghods and M. Herrmann, “A consistent rescaled momentum transport method for simulating large density ratio incompressible multiphase flows using level set methods,” *Phys. Scr.* **T155**, 014050 (2013).
- <sup>33</sup>S. J. Cummins, M. M. Francois, and D. B. Kothe, “Estimating curvature from volume fractions,” *Comput. Struct.* **83**, 425–434 (2005).
- <sup>34</sup>J. Smagorinsky, “General circulation experiments with the primitive equations: I. The basic experiment,” *Mon. Weather Rev.* **91**(3), 99–164 (1963).
- <sup>35</sup>A. J. Chorin, “Numerical solution of the Navier–Stokes equations,” *Math. Comput.* **22**, 745–762 (1968).
- <sup>36</sup>M. Rudman, “A volume-tracking method for incompressible multifluid flows with large density variations,” *Int. J. Numer. Methods Fluids* **28**, 357–378 (1998).
- <sup>37</sup>C. Liu and C. H. Hu, “An efficient immersed boundary treatment for complex moving object,” *J. Comput. Phys.* **274**, 654–680 (2014).
- <sup>38</sup>C.-W. Shu, “High-order finite difference and finite volume WENO schemes and discontinuous Galerkin methods for CFD,” *Int. J. Comput. Fluid Dyn.* **17**, 107–118 (2003).
- <sup>39</sup>R. D. Falgout and U. M. Yang, “hypr: A library of high performance preconditioners,” in *Computational Science—ICCS 2002. Lecture Notes in Computer Science*, edited by P. M. A. Sloot, A. G. Hoekstra, C. J. K. Tan, and J. J. Dongarra (Springer, Berlin/Heidelberg), Vol. 2331, pp. 632–641.
- <sup>40</sup>S. Balay, S. Abhyankar, M. Adams *et al.*, *PETSc Users Manual, Revision 3.8* (Argonne National Laboratory, Argonne, IL, 2017).
- <sup>41</sup>I. Wald, G. P. Johnson, J. Amstutz *et al.*, “Ospray—A CPU ray tracing framework for scientific visualization,” *IEEE Trans. Visualization Comput. Graphics* **23**, 931–940 (2017).
- <sup>42</sup>A. Witt, J. S. Gulliver, and L. Shen, “Numerical investigation of vorticity and bubble clustering in an air entraining hydraulic jump,” *Comput. Fluids* **172**, 162–180 (2018).
- <sup>43</sup>A. M. Castro, J. J. Li, and P. M. Carrica, “A mechanistic model of bubble entrainment in turbulent free surface flows,” *Int. J. Multiphase Flow* **86**, 35–55 (2016).
- <sup>44</sup>Y. Chachereau and H. Chanson, “Free-surface fluctuations and turbulence in hydraulic jumps,” *Exp. Therm. Fluid Sci.* **35**, 896–909 (2011).
- <sup>45</sup>P. Kumar, A. K. Das, and S. K. Mitra, “Bending and growth of entrained air filament under converging and asymmetric rotational fields,” *Phys. Fluids* **29**, 022101 (2017).
- <sup>46</sup>P. Kumar, A. K. Das, and S. K. Mitra, “Air entrainment driven by a converging rotational field in a viscous liquid,” *Phys. Fluids* **29**, 102104 (2017).
- <sup>47</sup>A. K. Roy and K. Kumar, “Experimental studies on hydrodynamic characteristics using an oblique plunging liquid jet,” *Phys. Fluids* **30**, 122107 (2018).
- <sup>48</sup>L. Deike, S. Popinet, and W. K. Melville, “Capillary effects on wave breaking,” *J. Fluid Mech.* **769**, 541–569 (2015).
- <sup>49</sup>K. T. Kiger and J. H. Duncan, “Air-entrainment mechanisms in plunging jets and breaking waves,” *Annu. Rev. Fluid Mech.* **44**, 563–596 (2012).
- <sup>50</sup>W. Chan, M. Dodd, P. Johnson *et al.*, “Formation and dynamics of bubbles in breaking waves: Part II. The evolution of the bubble size distribution and breakup/coalescence statistics,” Center for Turbulence Research Annual Research Briefs, 2018, pp. 21–34.
- <sup>51</sup>A. Khait and L. Shemer, “On the kinematic criterion for the inception of breaking in surface gravity waves: Fully nonlinear numerical simulations and experimental verification,” *Phys. Fluids* **30**, 057103 (2018).
- <sup>52</sup>C. Garrett, M. Li, and D. Farmer, “The connection between bubble size spectra and energy dissipation rates in the upper ocean,” *J. Phys. Oceanogr.* **30**, 2163–2171 (2000).
- <sup>53</sup>G. B. Deane and M. D. Stokes, “Scale dependence of bubble creation mechanisms in breaking waves,” *Nature* **418**, 839–844 (2002).
- <sup>54</sup>N. Mori and S. Kakuno, “Aeration and bubble measurements of coastal breaking waves,” *Fluid Dyn. Res.* **40**, 616 (2008).
- <sup>55</sup>M. Tavakolinejad, “Air bubble entrainment by breaking bow waves simulated by a 2D+ T technique,” Dissertation (University of Maryland, 2010).
- <sup>56</sup>F. Veron, C. Hopkins, E. L. Harrison *et al.*, “Sea spray spume droplet production in high wind speeds,” *Geophys. Res. Lett.* **39**, n/a, <https://doi.org/10.1029/2012GL052603> (2012).
- <sup>57</sup>D. Towle, “Spray droplet generation by breaking water waves,” Dissertation (University of Maryland, 2013).
- <sup>58</sup>H. Lhuissier and E. Villermaux, “Bursting bubble aerosols,” *J. Fluid Mech.* **696**, 5–44 (2012).